



HAL
open science

Evolution of the Comptonizing medium of the black-hole candidate Swift J1727.8–1613 along the hard to hard-intermediate state transition using NICER

Divya Rawat, Mariano Méndez, Federico García, Pierre Maggi

► To cite this version:

Divya Rawat, Mariano Méndez, Federico García, Pierre Maggi. Evolution of the Comptonizing medium of the black-hole candidate Swift J1727.8–1613 along the hard to hard-intermediate state transition using NICER. *Astronomy & Astrophysics - A&A*, 2025, 697, pp.A229. <10.1051/0004-6361/202453538>. <hal-05083188>

HAL Id: hal-05083188

<https://hal.science/hal-05083188v1>

Submitted on 24 May 2025

HAL is a multi-disciplinary open access archive for the deposit and dissemination of scientific research documents, whether they are published or not. The documents may come from teaching and research institutions in France or abroad, or from public or private research centers.

L'archive ouverte pluridisciplinaire **HAL**, est destinée au dépôt et à la diffusion de documents scientifiques de niveau recherche, publiés ou non, émanant des établissements d'enseignement et de recherche français ou étrangers, des laboratoires publics ou privés.



Distributed under a Creative Commons CC BY 4.0 - Attribution - International License

Evolution of the Comptonizing medium of the black-hole candidate Swift J1727.8–1613 along the hard to hard-intermediate state transition using NICER

Divya Rawat^{1,*}, Mariano Méndez^{2,*}, Federico García³, Pierre Maggi¹

¹ Observatoire Astronomique de Strasbourg, Université de Strasbourg, CNRS, 11 rue de l'Université, F-67000 Strasbourg, France

² Kapteyn Astronomical Institute, University of Groningen, PO BOX 800, Groningen NL-9700 AV, The Netherlands

³ Instituto Argentino de Radioastronomía (CCT La Plata, CONICET; CICPBA; UNLP), C.C.5, (1894) Villa Elisa, Buenos Aires, Argentina

Received 20 December 2024 / Accepted 5 April 2025

ABSTRACT

We analyse the properties of the Comptonizing medium in the black-hole X-ray binary Swift J1727.8–1613 using the time-dependent Comptonization model *vkompth*, applied to NICER observations of type-C QPOs in the hard and hard-intermediate states. During the 2023 outburst of the source, we measure the RMS and phase lags of the QPO across 45 observations as the QPO frequency, ν_{QPO} , evolves from ~ 0.3 Hz to ~ 7 Hz. By simultaneously fitting the time-averaged spectrum of the source and the RMS and lag spectra of the QPO, we derive the evolution of the disc and corona parameters. At $\nu_{\text{QPO}} = 0.34$ Hz, the QPO phase lags are hard, with 10 keV photons lagging 0.5 keV photons by ~ 0.5 rad. As ν_{QPO} increases, the lags for the same energy bands decrease, reaching near zero at $\nu_{\text{QPO}} \sim 1.2$ Hz, and then reverse to soft lags of ~ -1.1 rad at $\nu_{\text{QPO}} \sim 7$ Hz. Initially, the inner radius of the accretion disc is truncated at $\sim 30\text{--}40R_g$ (assuming a 10 solar-mass black hole) and, as the QPO frequency increases, the truncation radius decreases down to $\sim 10R_g$. Initially, two coronas of sizes of $\sim 6.5 \times 10^3$ km and $\sim 2 \times 10^3$ km, extend over the disc and are illuminated by different regions of the disk. As the QPO frequency increases, both the coronas shrink to $\sim 2 \times 10^3$ km at $\nu_{\text{QPO}} = 2.5$ Hz. Following a data gap, one corona expands again, peaking at a size of $\sim 2 \times 10^4$ km. We interpret the evolution of the coronal size in the context of accompanying radio observations, discussing its implications for the interplay between the corona and the jet.

Key words. accretion, accretion disks – black hole physics – methods: data analysis – stars: black holes – X-rays: binaries – X-rays: individuals: Swift J1727.8–1613

1. Introduction

Transient black hole X-ray binary (BHXB) systems generally remain in a quiescent state, exhibiting low X-ray flux levels. Before entering into outburst, they often show optical variability, which is seen as a precursor to the impending outburst (e.g., Hameury et al. 1997). During the outburst phase, these systems undergo notable X-ray flux variability across various energy bands (see, e.g., Remillard & McClintock 2006; Motta et al. 2012). The X-ray spectrum of these sources typically features a disc black-body component that dominates the low energies (Shakura & Sunyaev 1973), along with a power-law component that can extend up to ~ 1 MeV (Cadolle Bel et al. 2006). This non-thermal component is believed to result from the inverse Comptonization of seed-photons from the accretion disc (e.g. Gierlinski et al. 1997). Moreover, the spectra of these sources often include an iron emission line in the 6–7 keV range, the profile of which is used to probe the black-hole spin (e.g. Reynolds & Fabian 2008). Additionally, a Compton reflection hump is commonly observed around 20–30 keV (Basko et al. 1974; Magdziarz & Zdziarski 1995). Since these spectral components dominate distinct energy ranges, variability in flux or photon counts across these bands is frequently analysed to interpret changes in the system's accretion state.

Timing studies of various BHXBs have shown that these systems exhibit a hysteresis loop in the hardness-intensity diagram (HID) during outbursts (e.g. Homan et al. 2001). The accretion states are classified based on the source's position within the HID. In this context, the low-hard state (LHS) is identified by a high hardness ratio and low flux, while the high-soft state (HSS) features high flux and a low hardness ratio (Belloni et al. 2005; Done et al. 2007; Belloni et al. 2011, and references therein). Additionally, two intermediate states in between these two extreme states are recognised as the hard intermediate state (HIMS) and the soft intermediate state (SIMS). In the HSS the X-ray spectrum is dominated by blackbody disc emission, whereas the non-thermal component prevails in the LHS. The LHS spectrum is characterised by a power law with a photon index of approximately 1.5–2.0 (Gilfanov 2010), while the HSS includes a softer power-law component with a photon index of $\Gamma \geq 2.5$ (Méndez & van der Klis 1997; Remillard & McClintock 2006; Done et al. 2007).

Black hole X-ray binaries exhibit variability in their X-ray light curves, which we analyse in the Fourier domain using power density spectra (PDS, see van der Klis & Jansen 1985). The PDS reveal significant variability in BHXB across a wide range of timescales; the most important variability components are the quasi-periodic oscillations (QPOs, see Chen et al. 1997; Takizawa et al. 1997; Psaltis et al. 1999; Nowak 2000), categorised into mHz QPOs, low-frequency QPOs (LFQPOs), and

* Corresponding authors: rawat@unistra.fr, mariano@astro.rug.nl

High-Frequency QPOs (for a review, see [Ingram & Motta 2019](#), and references therein). LFQPOs occurring between 0.1 and 30 Hz, are further classified as Type-A, Type-B, and Type-C ([Wijnands et al. 1999](#); [Homan et al. 2001](#); [Remillard et al. 2002](#); [Casella et al. 2004](#)). Type-C QPOs are the most frequently observed, typically appearing in the LHS and HIMS (see [Motta et al. 2015](#), and references therein). In the PDS, these QPOs feature a large fractional root mean square (RMS) amplitude, often accompanied by a harmonic component at twice the QPO frequency, along with a broad Lorentzian noise component and occasionally a sub-harmonic component ([Belloni et al. 2002](#); [Casella et al. 2004](#)). Transient BXBs trace an oval-shaped wheel in the power colour-colour diagram, where the angle along the wheel (the hue) can be used to identify the canonical accretion states of these systems (see [Heil et al. 2015](#), for details).

Despite their prevalence in BHXB, the origin of these QPOs remains a subject of debate within the X-ray astronomy community, particularly between two prevailing models. One class of model considers that the LFQPOs are due to a geometric mechanism, as described by the relativistic precession model (RPM; [Stella & Vietri 1998](#); [Stella et al. 1999](#)), where the type-C QPO frequency would correspond to the Lense-Thirring precession frequency around the black hole ([Lense & Thirring 1918](#)). The RPM has been tested in BHXB systems such as GRO J1655–40 ([Motta et al. 2014a](#)), XTE J1550–564 ([Motta et al. 2014b](#)), and MAXI J1820+070 ([Bhargava et al. 2021](#), and references therein). An alternative class of models suggests a dynamical rather than a geometric mechanism for LFQPOs, including accretion-ejection instabilities in a magnetised disc ([Tagger & Pellat 1999](#)), oscillations in a transition layer within the accretion flow ([Titarchuk & Fiorito 2004](#)), and corona oscillations driven by magnetoacoustic waves ([Cabanac et al. 2010](#); [O’Neill et al. 2011](#)). In this context, LFQPOs have been associated with the relativistic dynamic frequency of a truncated accretion disc in BHXB such as GRS 1915+105 ([Misra et al. 2020](#); [Liu et al. 2021](#)), MAXI J1535–571 and H1743–322 ([Rawat et al. 2023a](#)), GX 339–4, and EXO 1846–031 ([Zhang et al. 2024](#)).

The timing and spectral properties of X-ray binaries have been widely used to investigate the physical and geometric characteristics of disk-corona systems, specifically through phase lags and RMS amplitude spectra at QPO frequencies ([Lee & Miller 1998](#); [Lee et al. 2001](#); [Kumar & Misra 2014](#)). This approach assumes that the flux oscillations in the time-averaged spectrum – modulated at the QPO frequency – are driven by oscillations in the thermodynamic properties of the Comptonizing region. These properties include the temperature and external heating rate of the corona, the electron density within the corona, and the temperature of the soft photon source, which provides seed-photons for Comptonization. [Karpouzas et al. \(2020\)](#) introduced `vkompth`, an improved model building on the earlier model by [Kumar & Misra \(2014\)](#) with enhanced equation-solving techniques. Originally designed for neutron star binaries, this model was later adapted for black-hole binaries as well ([Bellavita et al. 2022](#)). While this model describes the radiative properties of the QPO (RMS amplitude and lags) in terms of feedback loop between the corona and the disk, the same feedback mechanism can explain the QPO frequency ([Mastichiadis et al. 2022](#)). To date, the model has effectively explained comptonizing medium properties through type-A, type-B, and/or type-C QPOs in BHXB systems, including GRS 1915+105 ([Méndez et al. 2022](#); [García et al. 2022](#)), MAXI J1535–571 ([Zhang et al. 2022](#); [Rawat et al. 2023b](#); [Zhang et al. 2023a](#)), GRO J1655–40 ([Rout et al. 2023](#)),

MAXI J1820+070 ([Ma et al. 2023](#)), and MAXI J1348–630 ([García et al. 2021](#); [Zhang et al. 2023b](#); [Alabarta et al. 2025](#)).

Swift J1727.8–1613 (Swift J1727 hereafter) is a BHXB source first detected on August 24 2023 with Swift/BAT ([Page et al. 2023](#)) and initially classified as a GRB source but later identified as a BHXB source with MAXI/GSC ([Negoro et al. 2023](#)) and NICER ([O’Connor et al. 2023](#)). Using the GTC-10.4m telescope, [Mata Sánchez et al. \(2024\)](#) proposed that the companion star is an early K-type star and estimated an orbital period of ~ 7.6 h and a distance to the source of 2.7 ± 0.3 kpc. With the Very Long Baseline Array and the Long Baseline Array, [Wood et al. \(2024\)](#) imaged Swift J1727 during the hard/hard-intermediate state, revealing a bright core and a large, two-sided, asymmetrical, resolved jet. The polarization properties of Swift J1727 indicate that the source has an inclination angle between $30\text{--}60^\circ$ ([Veledina et al. 2023](#)).

During the initial phase of the outburst, observations with INTEGRAL, ART-XC, Swift/XRT, and AstroSat revealed a variable QPO in Swift J1727, with frequencies ranging from 0.8 Hz to 10.0 Hz ([Mereminskiy et al. 2024](#); [Nandi et al. 2024](#)). With IXPE, a QPO with a frequency evolving from approximately 1.3 Hz to 8.0 Hz was also reported in the 2–8 keV energy band by [Ingram et al. \(2024\)](#). Observations with IXPE and NICER from August to September 2023 showed that the source transitioned from the LHS to the HIMS, accompanied by a significant decrease in the polarization fraction from about 4% to 3% ([Ingram et al. 2024](#)). Using INTEGRAL/IBIS, [Bouchet et al. \(2024\)](#) reported a highly polarised spectral component above 210 keV, present in both the HIMS and the initial phases of the SIMS. Interestingly, during the HIMS, the polarization angle (PA) differs from the angle of the compact jet projected onto the sky, while in the SIMS the two angles are closely aligned ([Bouchet et al. 2024](#)). During the decay of the outburst, back in the LHS (during February 2024), the PA remained constant at the same value as at the one during the rising part, while the polarization fraction increased with X-ray hardness (4–8 keV/2–4 keV; [Podgorný et al. 2024](#)).

In this work, we analyse NICER observations of Swift J1727 during its LHS and HIMS to study the Comptonizing medium properties through the type-C QPOs using the `vkompth` model. In Section 2 we provide details of the observations, instrument specifications, and the spectral and timing analysis techniques applied. The fits to the RMS, lag and time-averaged spectra at the type-C QPO are presented in Section 3. We discuss the implications of these findings and interpret them within the disk-corona framework in Section 4.

2. Observations and data analysis

The Neutron Star Interior Composition Explorer (NICER), launched on June 2, 2017, is mounted on the International Space Station ([Gendreau et al. 2016](#)). Its X-ray Timing Instrument operates within the 0.2–12.0 keV energy range, with an effective area exceeding 2000 cm² at 1.5 keV. NICER provides an energy resolution of 85 eV at 1 keV and a time resolution of 4×10^{-8} s. We used NICER observations of Swift J1727 from 2023-08-26 to 2023-10-09, with observation details presented in Table A.1.

We processed each observation using the `nicer12` task, applying standard calibration and screening procedures. By default, `nicer12` uses the ‘night’ threshold setting, but there are observations with no exposure during the night; for those observations, we set `threshfilter=DAY`. We used either day or night data for an individual observation, because NICER has been

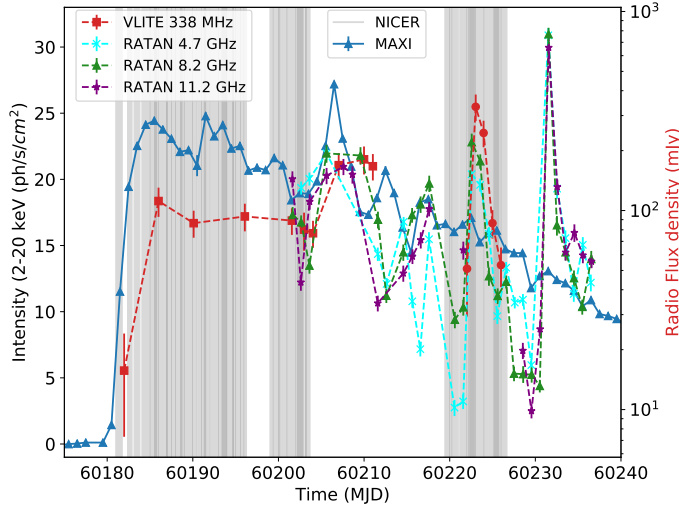


Fig. 1. MAXI light curve of Swift J1727.8–1613 starting from 60175 MJD (August 19, 2023) in the 2–20 keV energy band in units of photons $s^{-1} cm^{-2}$ (blue triangles; left y axis). The right y-axis shows the radio flux density in mJy from the VLA Low-band Ionosphere and Transient Experiment (VLITE) at 338 MHz (red data points, data from Peters et al. 2023), alongside RATAN-600 observations at frequencies of 4.7 GHz (cyan data points), 8.2 GHz (green data points), and 11.2 GHz (purple data points, data from Ingram et al. 2024).

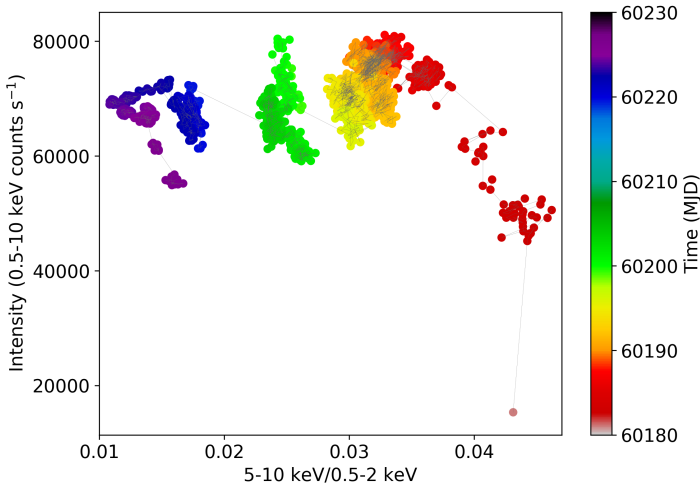


Fig. 2. NICER hardness-intensity diagram starting from MJD 60181. The intensity is the 0.5–10.0 keV count rate and the hardness is the ratio of the count rate in the 5–10 keV band to that in the 0.5–2.0 keV band, with data points binned over 100 seconds. The colour scale indicates the MJD.

affected by optical light leakage on May 2023 and hence separate analysis of orbit day and orbit night data is recommended by the NICER team¹. We only used observations where the exposure time is greater than 200 seconds after running the `nicer12` task. Next, we extracted light curves in the 0.3–4.0 keV, 8.0–12.0 keV, and 0.5–10.0 keV energy bands using the `nicer13-1c` task. The left panel of Figure 1 shows the MAXI light curve for Swift J1727, with NICER observations highlighted in the shaded grey regions. Details of the NICER count rates are provided in Appendix Table A.1. We then calculated the hardness ratio as the number of photons in the 5.0–10.0 keV band divided by those

in the 0.5–2.0 keV band. We segment the observations where a significant change in both the full-band count rate and hardness ratio was observed. To illustrate the source evolution, we plot the HID using NICER data in the Figure 2. The colour scale on the right side of that Figure represents time, with red corresponding to MJD 60181 and transitioning to navy blue at MJD 60226, 45 days later.

2.1. Timing analysis

We extracted the fractional RMS normalised (Belloni & Hasinger 1990) PDS and cross spectrum for each observation using the General High-energy Aperiodic Timing Software (GHATS)² V3.1.0. We used the novel technique proposed by Méndez et al. (2024) to measure the phase lags. For each observation, we first extracted the 0.5–10.0 keV PDS and the cross spectrum between the 0.5–2.0 keV and 2.0–10.0 keV energy bands. We fit the PDS with a combination of Lorentzian functions together with the real and imaginary parts of the cross spectrum. For each component present in the PDS, we fit the real and imaginary part of the cross spectrum with Lorentzians multiplied by $\cos(\Delta\phi)$ and $\sin(\Delta\phi)$, respectively with the centroid and width of each Lorentzian tied to the parameters in the PDS, where $\Delta\phi$ is the phase lag.

We observe that the QPO centroid frequency varies from 0.3 Hz to 7.0 Hz (Appendix Table A.1). For some observations marked with a * in Appendix Table A.1, the QPO detection was below 3 sigma, so these observations were excluded from further analysis. Additionally, for obs no. 3 and 4, the QPO was weak in the 0.5–10.0 keV band, and therefore, these observations were also excluded from further study. To measure the phase-lag and RMS spectra, we divide the energy bands into 38 bins, starting from 0.5 keV to 7.9 keV with a bin size of 0.2 keV, and a last bin that spans from 7.9 keV to 10 keV due to the QPO being weaker in the highest energy band. For some observations (mainly those where we segmented the observation into parts or the QPO frequency exceeded 2.5 Hz), the QPO fractional RMS was low (as shown in Appendix Table A.1), making the QPO insignificant with finer binning. To address this in those observations, we manually merge the bins in regions where the signal was weak, resulting in 11 energy bands: 0.5–0.9 keV, 0.9–1.3 keV, 1.3–1.7 keV, 1.7–2.1 keV, 2.1–2.9 keV, 2.9–3.7 keV, 3.7–4.5 keV, 4.5–5.7 keV, 5.7–6.5 keV, 6.5–7.7 keV, and 7.7–10.0 keV. For each band we extract the phase lag and RMS using the technique of Méndez et al. (2024) discussed above using the 0.5–10.0 keV band as the reference. To account for the correlation due to photons being present in both the subject and reference bands, we include a constant term in the model of the real part of the cross-spectrum.

2.2. Spectral analysis

We used the `nicer13-spect` task to extract source and background spectra, response (`rmf`) and ancillary response (`arf`) files in the 0.5–10.0 keV band. We used Heasoft version 6.33 and CALDB version 20240206. We fitted the background-subtracted time-averaged spectrum of the source using the model `TBfeo*(diskbb + gaussian + nthComp)` in Xspec 12.14.0. The `TBfeo` model is similar to the `tbabs` model, which accounts for interstellar absorption, but allows the oxygen and iron abundances to vary, in addition to the hydrogen

¹ https://heasarc.gsfc.nasa.gov/docs/nicer/analysis_threads/nicer12/

² http://www.brera.inaf.it/utenti/belloni/GHATS_Package/Home.html

column density. We used the cross-section tables of Verner et al. (1996) and the abundances of Wilms et al. (2000) and left the hydrogen column density as a free parameter. We have frozen the oxygen and iron abundance relative to Solar to 1 and the redshift to zero. The diskbb component models the thermal emission from an optically thick and geometrically thin accretion disc (Mitsuda et al. 1984; Makishima et al. 1986) while nthcomp (Zdziarski et al. 1996; Życki et al. 1999) models the Comptonised emission from the X-ray corona. We kept both diskbb parameters, the temperature at the inner disc radius, kT_{in} , and the normalisation free. The nthcomp model parameters are the power-law photon index, Γ , electron temperature, kT_e , seed-photon temperature, kT_{bb} , and normalisation. The seed-photon temperature kT_{bb} was tied to kT_{in} of the diskbb component. Since the electron temperature of nthcomp could not be constrained with the NICER data, following Bouchet et al. (2024) we fixed it at 40 keV for observations 2 to 36 and at 250 keV for observations 37 to 54. We modelled the relatively broad iron line present in the residuals of observations 1 to 17 with a Gaussian fixed at 6.4 keV using the gauss model.

2.3. Time-dependent Comptonization model

To study the properties of the Comptonizing medium, we model the RMS and phase-lag spectra of the QPO with the time-dependent Comptonization model vkompth³. The time-averaged variant of vkompth model is identical to the thermal Comptonization model nthComp, but vkompth incorporates additional parameters that only impact the time-dependent version of the model. In the case of a disk-blackbody soft photon-source, the vkompth model has two versions: one for a single corona, vkompthdk, and second for a dual corona, vkdua1dk. The model parameters for vkompthdk are the seed-photon temperature, kT_s , the electron temperature, kT_e , the photon index, Γ , the corona size, L , the feedback fraction, η , the size of the seed-photon source, a_f , the amplitude of the variability of the external heating rate, $\delta\dot{H}_{\text{ext}}$, and the reference lag of the model in the 0.5–10.0 keV energy band, reflag . Since the vkompth model is not sensitive to a_f , we fix this parameter at 250 km (for details, see García et al. 2022). The parameter reflag is an additive normalisation that allows the model to match the data, given that the observer is free to choose the reference energy band of the lags. The vkdua1dk model (García et al. 2021; Bellavita et al. 2022) has two sets of coronal parameters, $kT_{s,1}/kT_{s,2}$, $kT_{e,1}/kT_{e,2}$, Γ_1/Γ_2 , L_1/L_2 , η_1/η_2 , and $\delta\dot{H}_{\text{ext},1}/\delta\dot{H}_{\text{ext},2}$ to describe the physical properties of the two coronal regions. The remaining parameters of the dual models are the size of the seed-photon source and the reference lag, plus an additional parameter, ϕ , which describes the phase difference between the two coupled coronae (for more details see García et al. 2021). To model the RMS spectra of the QPO, we incorporate a multiplicative dilution component, which is a function of energy (E). This component accounts for the fact that the RMS amplitude we observe is diluted by the emission of the other components that we assume do not vary (see details in Bellavita et al. 2022). We linked the parameters of the dilution component to the corresponding parameter of the model of the time-averaged spectrum. We will discuss the results of the fit in detail in Section 3.2.

³ <https://github.com/candebellavita/vkompth>

3. Results

We present the MAXI light curve of Swift J1727 during its outburst in August 2023 in Figure 1. To show the simultaneous evolution of the source in radio, we over-plot the radio light curves obtained from the VLA Low-band Ionosphere and Transient Experiment (VLITE) 338 MHz (data from Peters et al. 2023), along with the RATAN-600 observations at 4.7 GHz, 8.2 GHz and 11.2 GHz (data from Ingram et al. 2024). The MAXI flux in the 2–20 keV band rises from ~ 0.5 photons $\text{s}^{-1} \text{cm}^{-2}$ to ~ 25 photons $\text{s}^{-1} \text{cm}^{-2}$ over a period of 5 days, starting from MJD 60180 (August 24, 2023). The VLITE light curve shows a significant increase in radio flux starting from MJD 60181.98 that remains more or less constant until MJD 60204.04. The X-ray flux then decreases to ~ 5 photons $\text{s}^{-1} \text{cm}^{-2}$ over nearly two months, with several X-ray and radio flares occurring in between. The VLITE data show two radio flares on MJD 60209.99 and MJD 60223.04, while a very bright radio flare is visible in the RATAN-600 data at 4.7 GHz, 8.2 GHz, 11.2 GHz frequencies on MJD 60231.54. We mark the times of the NICER observations with grey regions in Figure 1. The NICER 0.5–10.0 keV count rate initially increases from $\sim 1.5 \times 10^4$ counts s^{-1} to $\sim 7.5 \times 10^4$ counts s^{-1} . Simultaneously, the HR of the source decreases from ~ 0.045 to ~ 0.035 , indicating a clear evolution from the LHS to the HIMS as shown in Figure 2. The HR decreases further from approximately ~ 0.035 to ~ 0.015 , while the flux continues to decrease monotonically, reaching around $\sim 5.7 \times 10^4$ counts s^{-1} .

3.1. Timing results

Adopting the method of Belloni et al. (2002), we fit the PDS with four to five Lorentzian components. Following Méndez et al. (2024), we used the same combination of Lorentzians to fit the real and imaginary parts of the cross spectra multiplied by, respectively, the cosine and sine of the phase lags which, for each individual Lorentzian, are assumed to be constant with frequency. During the fits we link the frequencies and full width at half maximum of each Lorentzian in the PDS and cross spectra. The model includes two components that represent the broadband noise: (1) a zero-centred Lorentzian representing the low frequency broad-band noise and (2) a high-frequency broad noise component around 11.0 Hz. To fit the narrow peak components, which we identify as the QPO and its second harmonic, we used two separate Lorentzians. While fitting the harmonic component, we set the Lorentzian centroid frequency and width to twice the corresponding values of the QPO fundamental. For QPO centroid frequencies of less than 3.0 Hz, the PDS also shows a low-frequency noise component (see, for example, the top left panel of Figure 3). We include an additional Lorentzian to account for this feature whenever required.

We show the fit to the PDS and the real and imaginary part of the cross spectrum of OBSID 6203980105 in Figure 3. The top left panel shows the PDS and the right panel shows the residuals of the fit. The PDS shows a significant narrow QPO component at ~ 0.89 Hz with a harmonic component at twice that frequency. On the basis of strength of the QPO and the presence of a harmonic, and broad noise components, we identify this as a type-C QPO. In the middle left and bottom left panels of Figure 3, we display the real and imaginary parts of the cross spectrum, along with the corresponding residuals of the fit in the middle and bottom-right panels. For ObsID 6557020402, which features a QPO at approximately 7.0 Hz, we present the PDS and the real and imaginary parts of the cross spectrum in Appendix Figure A.1. The real part of the cross spectrum

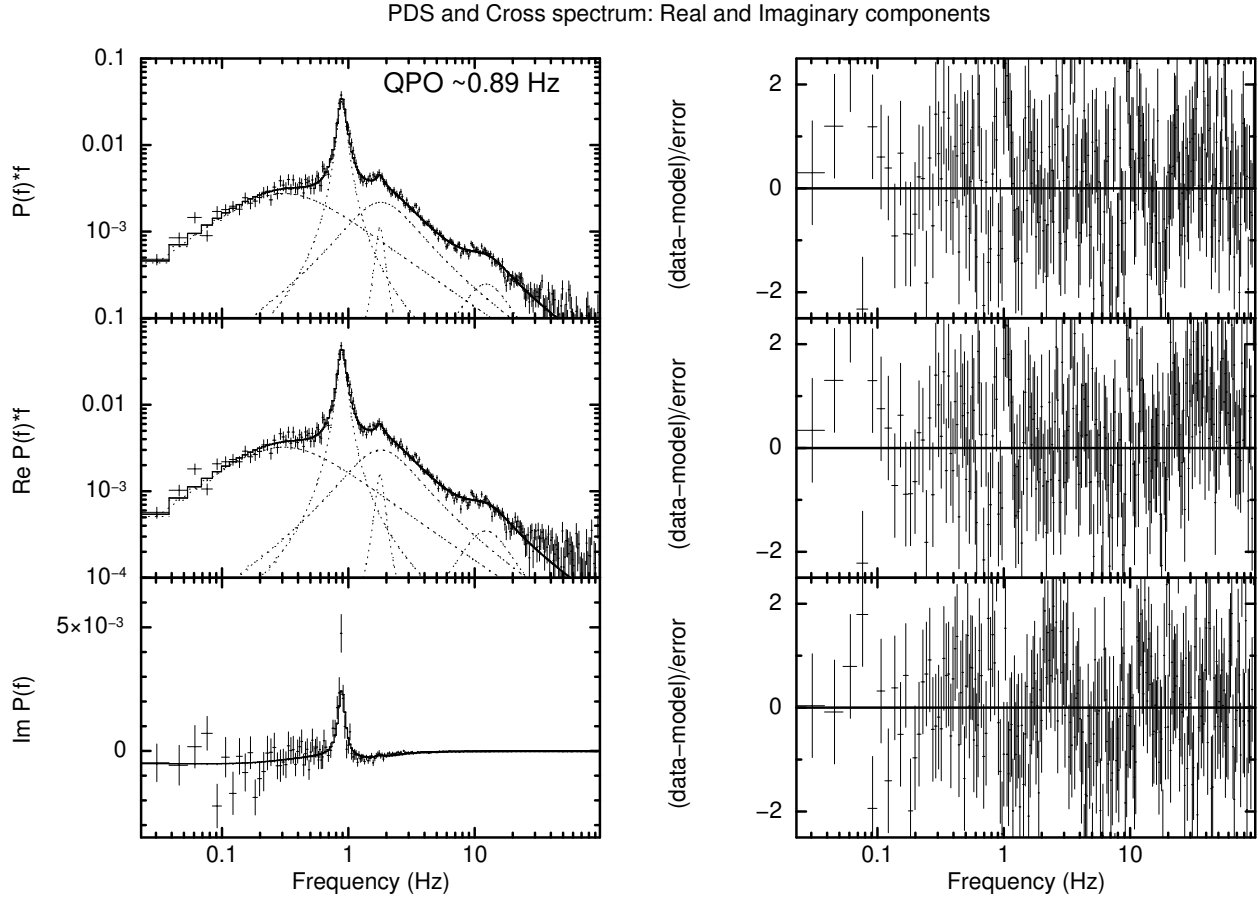


Fig. 3. Top left panel displays the 0.5–10.0 keV power density spectrum of Swift J1727.8–1613, fitted with five Lorentzians for ObsID 6203980105. The middle and bottom left panels show the real and imaginary parts of the cross spectrum between the 0.5–2.0 keV and 2.0–10.0 keV bands, along with the best-fitting model that assumes that the phase lags of each Lorentzians are constant with Fourier frequency (see Méndez et al. 2024). The right-hand panels display the residuals of the fits for the respective spectra.

contains the same number of Lorentzians as the PDS. Meanwhile, the imaginary part shifts from positive to negative as the QPO frequency increases from 0.3 to 7.0 Hz (see bottom left panel of Figure 3 and Appendix Figure A.1).

The QPO frequency increases monotonically from 0.3 Hz to 1.4 Hz over time until MJD 60196, as shown in Figure 4 (see also Appendix Table A.1). Between MJD 60199 and MJD 60201, the QPO frequency abruptly increases from 2.3 Hz to 3.3 Hz, then drops to 2.0 Hz within a span of just one day. The QPO frequency then increases further to 7.0 Hz, with a gap in NICER data between MJD 60203 and MJD 60219. The colour scale on the right side of the Figure indicates the QPO fractional RMS in the 0.5–10.0 keV band. The QPO fractional RMS first increases from 7.6% to 9.3% as the QPO frequency increases from ~ 0.3 Hz to ~ 0.8 Hz, and then decreases from 9.3% to $\sim 1\%$ as the QPO frequency increases from ~ 1 Hz to ~ 7 Hz at the end of the NICER observations (see also Appendix Table A.1). During the period, where the QPO frequency exhibits an abrupt increase and then decreases, the fractional RMS remains anti correlated. This behaviour of the fractional RMS is similar to that observed in other BHXB sources like GRS 1915+105 (Zhang et al. 2020), and MAXI J1535–571 (Rawat et al. 2023b). We give details of the QPO centroid frequency, width and fractional RMS in the 0.5–10.0 keV band in Appendix Table A.1.

We show the QPO phase lag spectra at five QPO frequencies, 0.34 Hz, 0.79 Hz, 1.22 Hz, 2.56 Hz, 6.19 Hz, and 7.02 Hz, in Figure 5. At a QPO frequency of 0.34 Hz, the phase lags are neg-

ative at low energies and become positive at ~ 1.5 keV, continue increasing and become more or less constant at 0.25 rad above ~ 3 keV. The lags increase with energy when $\nu_{\text{QPO}} \leq 0.34$ Hz, flatten for $0.79 \text{ Hz} < \nu_{\text{QPO}} \leq 2.56$ Hz, and decrease with energy when $\nu_{\text{QPO}} \geq 6.19$ Hz. Additionally, the lags show minima that shift to higher energies as a function of QPO frequency. At $\nu_{\text{QPO}} = 0.34$ Hz, the minimum appears between 0.5 and 1.0 keV; for $0.79 \text{ Hz} < \nu_{\text{QPO}} \leq 2.56$ Hz, the minimum shifts to 1.5–2.0 keV, and by $\nu_{\text{QPO}} \geq 6.19$ Hz, the minimum is at around 4 keV. A similar shift in the phase-lag spectra minima is also observed for the type-B QPOs in MAXI J1348–630 and for the type-C QPOs in MAXI J1535–571 (Rawat et al. 2023b). We also computed the time lag of the 2.0–10.0 keV band with respect to 0.5–2.0 keV band, across all observations (see the second row of Appendix Tables A.2, A.3, A.4 and A.5).

3.2. Spectral-timing results

We fit simultaneously the RMS spectrum of the QPO with the model `vkompthdk*dilution`, the phase-lag spectrum of the QPO with the model `vkompthdk` and the time averaged spectrum of the source with model described in Section 2.2. We tie kT_e and Γ of `vkompthdk` to kT_e and Γ of `nthcomp`, and link all other parameters of `vkompthdk` between the lag spectra and the RMS spectra. While fitting the `vkompthdk` model, we initially tied the diskbb temperature (kT_{in}) to the seed photon temperature (kT_s) of `vkompthdk`. However, the model was unable

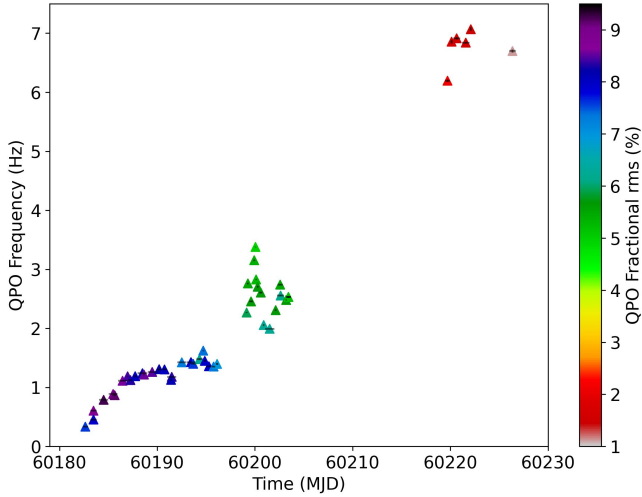


Fig. 4. QPO frequency of Swift J1727.8–1613 as a function of MJD. The colour bar gives the QPO fractional RMS amplitude in the 0.5–10.0 keV energy range.

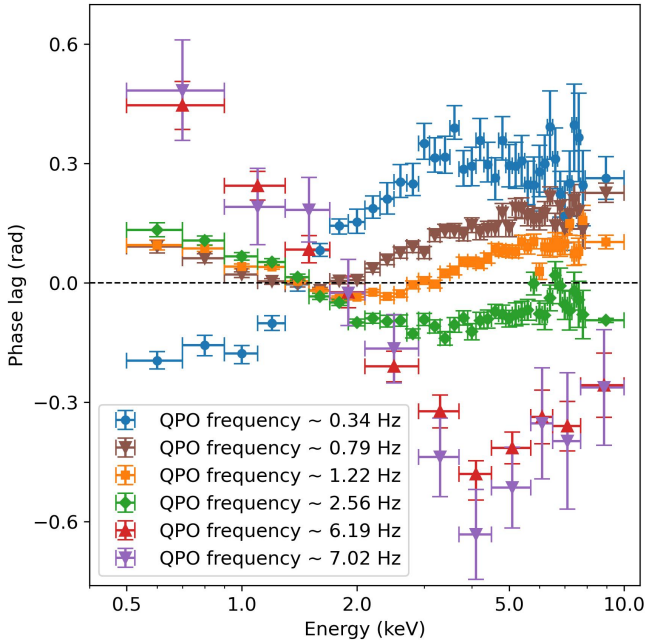


Fig. 5. Phase-lag spectra corresponding to specific QPO frequencies, from 0.34 Hz to 7.02 Hz. The reference energy band used here for the lags is 0.5–10.0 keV.

to reproduce the valley in the phase lag spectrum and gives a $\chi^2/\text{d.o.f.}$ of 1748.1/253. A similar behaviour was observed in the black hole X-ray binary MAXI J1535–571 when modelled with `vkompthdk`, where the fit improves significantly when kT_{in} and kT_s were untied (see Figure 6 of Rawat et al. 2023b). To address this, we allowed kT_{in} and kT_s to vary independently, and found two separate sources of seed photon; one with a temperature of $kT_{in} \sim 0.35$ keV, responsible for producing the steady-state spectra, and another with a temperature of $kT_s \sim 0.06$ keV, which contributes to the phase lag and RMS spectra. As an example, we show the time averaged spectrum of the source fitted with the model `TBfeo*(diskbb + gaussian + nthComp)`, and the RMS and phase-lag spectra of the QPO at 0.89 Hz fitted with the model `vkompthdk*dilution` and `vkompthdk` in,

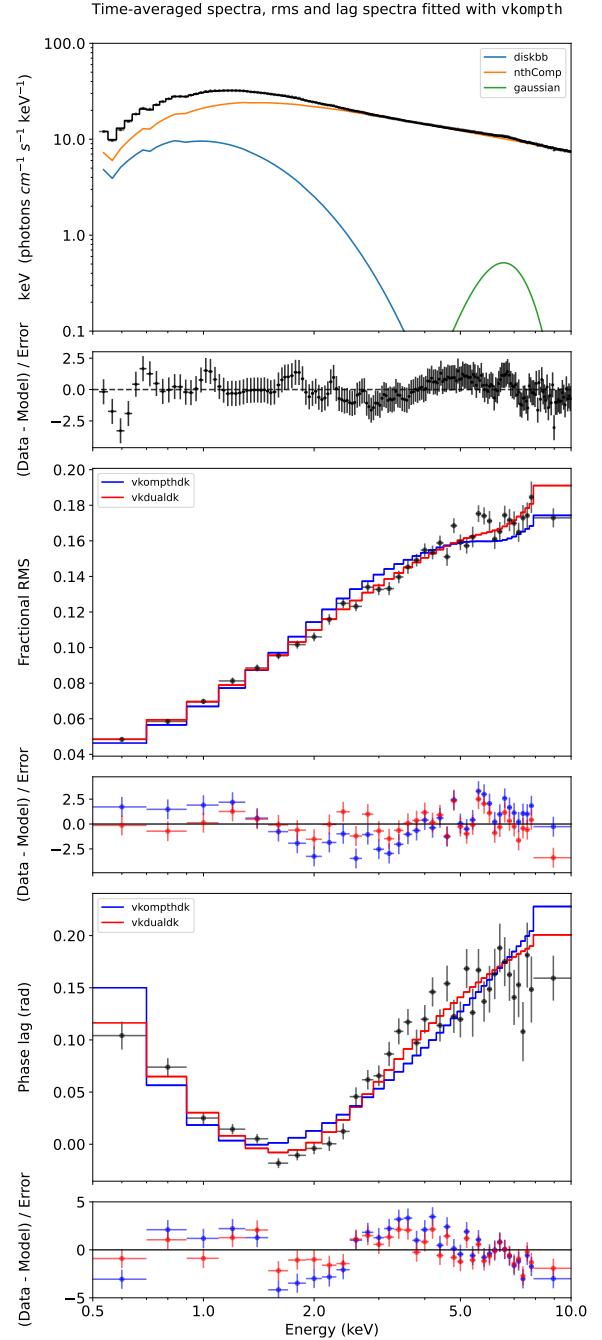


Fig. 6. Top panel shows the NICER time-averaged spectrum of Swift J1727.8–1613 (ObsID 6203980105) with a QPO centroid frequency of 0.89 Hz, fitted using the model `TBfeo*(diskbb + gaussian + nthComp)` together with the residuals of the best-fitting model. The middle panel shows the RMS spectrum of the QPO fitted with the `vkdualdk*dilution` (red) and `vkompthdk*dilution` (blue) models with the residuals of the best-fitting model. The bottom panel shows the phase-lag spectrum of at the QPO fitted with the `vkdualdk` (red) and `vkompthdk` model (blue) with the residuals of the best-fitting model. The 0.5–10.0 keV energy band is used as the reference for the phase-lag spectra.

respectively, the top, middle and bottom panels of Figure 6, with the `vkompthdk` model plotted in blue in the middle and bottom panels (obs no. 6). As it appears from the Figure, `vkompthdk` still cannot fit the minimum of the phase-lag spectra properly,

Table 1. Representative best-fitting spectral and corona parameters for ObsID 6203980105 of Swift J1727.8–1613 using the single and dual corona model.

Component	Parameter	M1 ⁽¹⁾	M2 ⁽²⁾
TBfeo	$N_{\text{H}}(10^{22} \text{ cm}^{-2})$	[0.28] ^a	[0.28] ^a
diskbb	kT_{in} (keV)	0.351 ± 0.003	0.352 ± 0.003
	N_{disk} (10^4)	15.8 ± 0.2	15.7 ± 0.4
nthComp	Γ	1.742 ± 0.002	1.742 ± 0.003
	kT_e (keV)	[40] ^a	[40] ^a
	N_{nthComp}	$34.4^{+0.3}_{-0.2}$	34.4 ± 0.3
gaussian	LineE (keV)	[6.4] ^a	[6.4] ^a
	σ (keV)	[1.0] ^a	[1.0] ^a
	Strength (10^{-1})	[0.2] ^a	[0.2] ^a
vkompthdk/vkdualdk	$kT_s / kT_{s,1}$ (keV)	0.057 ± 0.001	$0.286^{+0.020}_{-0.055}$
	L / L_1 (10^3 km)	31.4 ± 0.7	$6.1^{+1.5}_{-1.3}$
	L_2 (10^3 km)	–	$7.5^{+2.1}_{-1.7}$
	η / η_1	$0.60^{+0.03}_{-0.02}$	$0.28^{+0.02}_{-0.04}$
	η_2	–	0.32 ± 0.01
	ϕ (rad)	–	3.11 ± 0.01
	reflag (10^{-2})	3.1 ± 0.2	8.2 ± 0.5
	$\eta_{\text{int},1}$	0.013 ± 0.001	$0.014^{+0.003}_{-0.002}$
	$\eta_{\text{int},2}$	–	0.017 ± 0.001
	χ^2 (d.o.f.)	415.2 (255)	254.2 (251)

Notes. Uncertainties are given at the 1σ level. ⁽¹⁾ In Model M1, the RMS spectra are fitted with vkompthdk*dilution, while the lag spectra are fitted with vkompthdk. ⁽²⁾ In Model M2, the RMS spectra are fitted with vkdualdk*dilution, while the lag spectra are fitted with vkdualdk. ^(a) The parameters N_{H} and LineE are frozen.

yielding a chi-square of 415.2 for dof 255 (see Table 1 for best fit parameters).

Next we fit the RMS spectra of the QPO with the model vkdualdk*dilution (Karpouzas et al. 2020; Bellavita et al. 2022) and the lag spectra of the QPO with the model vkdualdk. We tie $kT_{e,1}/kT_{e,2}$ of vkompthdk to kT_e of nthcomp, Γ_1/Γ_2 of vkompthdk to Γ of nthcomp, and link all the parameters of vkompthdk between the lag spectra and the RMS spectra. We allowed the seed photon temperature of the first corona, $kT_{s,1}$, to vary independently, while tying the seed photon temperature of the second corona, $kT_{s,2}$, to the inner disc temperature, kT_{in} . The chi-square for the fit with a dual-corona model decreases to 254.2 for dof 251 (obs no. 6). We give the best-fitting parameters for obs no. 6 in Table 1 along with the chi-square of the fits for both models. In the middle and bottom panels of Figure 6, the solid red line represents the best fit model of vkdualdk*dilution and vkdualdk to, respectively, the RMS and phase-lag spectra of the QPO. The corner plot of the spectral parameters for obs no. 6, generated using pyXspecCorner⁴, is shown in Figure A.3. During the period MJD 60181–60199, the phase-lag spectra at the QPO frequency are flat ($1.0 \text{ Hz} < \nu_{\text{QPO}} < 2.5 \text{ Hz}$). The phase lag spectra are reasonably well-fitted by the single-corona model vkompthdk; however, when a valley is evident in the lag spectra (see Figure 5), fits using the dual-corona model, vkdualdk, provide statistically better results.

For most observation in the period MJD 60199–60203 (obs. 28–42), the dual-corona model appears to over-fit the data, while the single-corona model provides statistically acceptable fits. For instance, in observation 32, the single-corona model yields $\chi^2/\text{d.o.f.} = 115.7/153$. In these cases, the over-fitting of the dual-corona model may be explained by the decreasing QPO RMS amplitude over time or, in some cases, by shorter exposure times, which result in the RMS and lag spectra being less able to constrain the model parameters. Nevertheless, even in cases where the dual-corona model over-fit the data, the sizes of the two coronas remain consistent with each other, similar to the earlier period. For the few observations in this period where the dual-corona model still provides a statistically better fit (see Tables A.2–A.5), the sizes of the two coronas again remain in good agreement. To avoid inconsistencies in our analysis by switching between single and dual-corona models, we opt to fit all observations in with the dual-corona model. In cases where the dual-corona model over-fits the data, we link the sizes of the two coronas to be the same, ensuring a coherent and systematic approach to the modelling.

After the data gap between observations 42 (MJD 60203.4) and 43 (MJD 60219.7), the size of the second corona can no longer be constrained when fitting with the dual-corona model. We initially tied the parameters of the two coronas, but since the lag is not flat in these observations, unlike in previous ones, the single-corona model could not produce the valley in the lag spectrum. First, we tied the sizes of both coronas (L_1 and L_2), which resulted in a reduced chi-square of 143.0/174 as shown in Figure A.2 (solid blue line). While this is statistically a good fit, the model still did not reproduce the observed phase lag valley. Next, we let the two corona sizes vary separately, but we were unable to constrain L_2 , likely due to the limited number of bins in those observations. We then fixed L_2 to the value obtained in observation 39, the last one where the second corona can be reliably measured ($L_2 = 1.9 \times 10^3$ km). This gives a $\chi^2/\text{d.o.f.}$ of 128.5/173 and the model fits the valley of the phase lag spectra as shown by the solid red line in Figure A.2.

From the fits to the time-averaged spectrum of the source and the RMS and phase lag spectra of the QPO, we find that during the hard and hard-intermediate states, the inner disc temperature, kT_{in} , increases from ~ 0.27 keV to ~ 0.73 keV with time as shown in the left panel of Figure 7. The power-law index increases from ~ 1.6 to ~ 3.0 , which highlights the evolution of the source from the hard to the hard-intermediate state during the course of the observations, as shown in the right panel of Figure 7. The coronal seed temperature, $kT_{s,1}$ also increases from ~ 0.25 keV to ~ 0.70 keV. We show the evolution of $kT_{s,1}$ in the top left panel of Figure 7. The kT_{in} , $kT_{s,1}$ and power-law index increase and then decrease as a function of time between MJD 60199 and MJD 60201.

Using the parameters of vkdualdk we have computed the intrinsic feedback fraction, the fraction of the corona flux, $\eta_{\text{int},1}$ and $\eta_{\text{int},2}$, that returns to the disc (see Karpouzas et al. 2020 for details) from corona 1 (C_1) and corona 2 (C_2), respectively (given in Appendix Tables A.2–A.5). We show $\eta_{\text{int},1}$ and $\eta_{\text{int},2}$ as a function of time with the black and blue points in the bottom left panel of Figure 7, respectively. The intrinsic feedback fraction for both coronas is ~ 2 – 5% when the QPO frequency is in the range 0.3–2.6 Hz. When the QPO frequency is above 2.6 Hz, the feedback fraction rises to ~ 15 – 20% for corona 1 and to $\sim 10\%$ for corona 2. We note that we have frozen the value of the feedback fraction in obs. 17, because it remained unconstrained otherwise.

⁴ <https://github.com/garciafederico/pyXspecCorner>

Variations of spectral parameters as a function of time

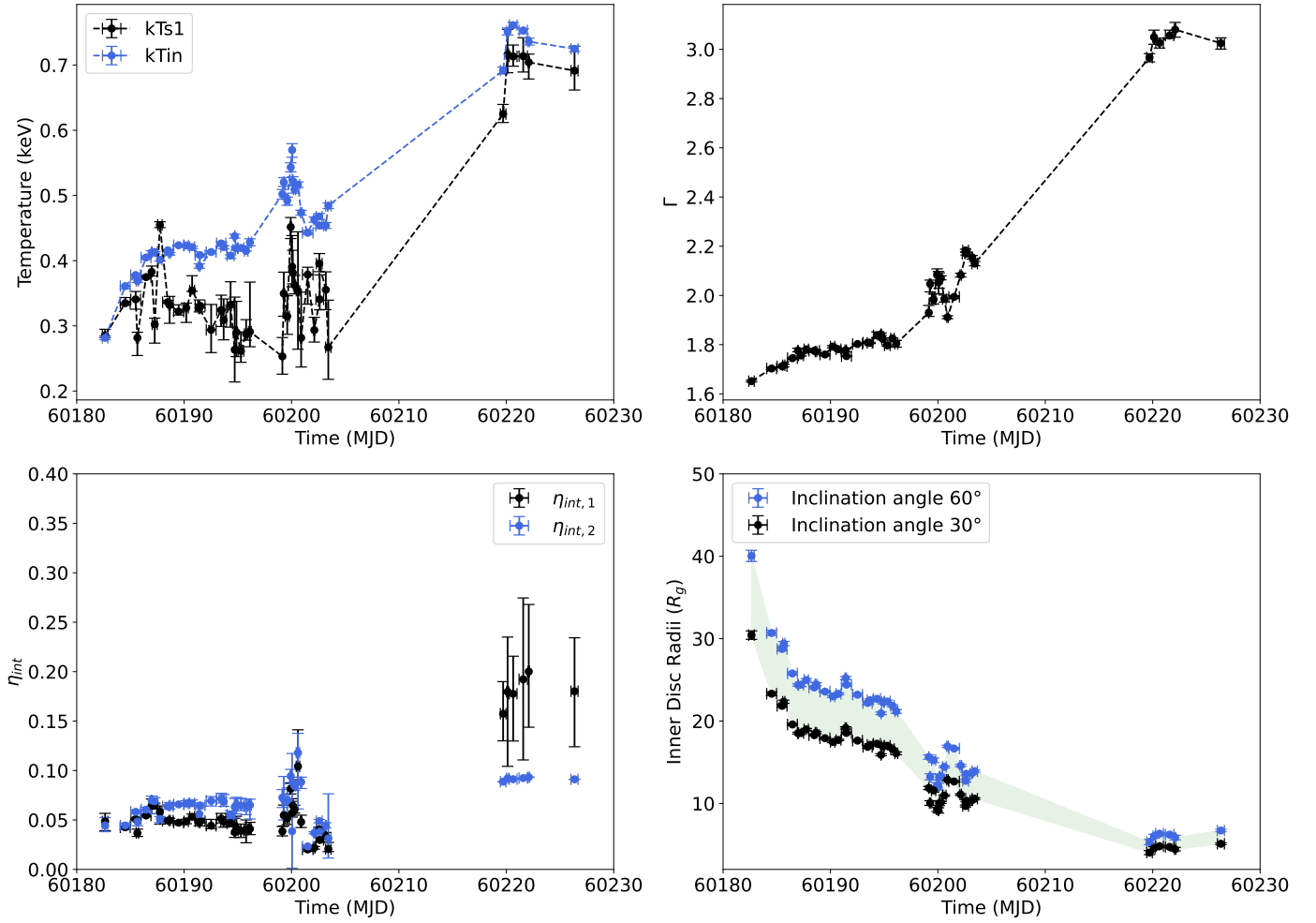


Fig. 7. Top left panel shows the inner disc temperature, kT_{in} , and coronal seed temperature, $kT_{s,1}$, as a function of time for Swift J1727.8–1613. The top right panel presents the power-law photon index of NTHCOMP, Γ , as a function of time. The bottom left panel displays the time evolution of the intrinsic feedback fraction, $\eta_{int,1}$ and $\eta_{int,2}$, obtained from the fit with the vkualdk model. The bottom right panel shows the evolution of the inner disc radius (in units of gravitational radii) for inclination angles of 60° (blue) and 30° (black). For the calculation of the inner disc radius, we used a spectral hardening factor T_{col}/T_{eff} of 1.7, assumed a M_\odot black hole, and set the distance to the source at 2.7 kpc.

Assuming that the source is at a distance of 2.7 kpc (Mata Sánchez et al. 2024) and has an inclination angle between 30° – 60° (Veledina et al. 2023), we translate the diskbb norm parameter (given in Appendix Tables A.2–A.5) to an inner disc radius, including a spectral hardening factor T_{col}/T_{eff} of 1.7 (Shimura & Takahara 1995; Kubota et al. 1998). Assuming that the system harbours a $10 M_\odot$ black hole, we compute the inner disc radii range in units of the gravitational radius, $R_g = GM/c^2$, as shown in the bottom right panel of Figure 7 as a function of time. The shaded green region in Figure 7 shows that the inner disc radius decreases from 30 – $40 R_g$ to 5 – $7 R_g$ as the QPO frequency increases from 0.3 to 7.0 Hz.

The analysis reveals that, as the QPO frequency increases from 0.3 Hz to 2.5 Hz, L_1 decreases from $\sim 6.5 \times 10^3$ km to $\sim 2 \times 10^3$ km with some fluctuations in between as shown in Figure 8. During the first observation, L_2 starts at approximately $\sim 2 \times 10^3$ km, expands to around $\sim 8 \times 10^3$ km, and then contracts to nearly the same values as L_1 . For the first observation L_2 is $\sim 2 \times 10^3$ km, it then expands to $\sim 8 \times 10^3$ km and then contracts to a size that is nearly equal to L_1 . This trend is also consistent with the results of Liao et al. (2024), which fit the vkompthdk model between MJDs 60198 to 60203 and find that the size of corona

decreases from ~ 2500 km to ~ 1000 km and then increases again to ~ 2000 km. After a gap of about two weeks in the data, the QPO is at frequency of ~ 6 Hz. Assuming no further variation in the size of the second corona in the observations with QPO frequency in the 6–7 Hz range, which we fixed to 1.9×10^3 km (see previous paragraph), the size of the first corona increases again, from $\sim 2 \times 10^3$ km to $\sim 10 \times 10^3$ km at 6.0 Hz, and further to $\sim 15 \times 10^3$ km when the QPO frequency reaches 7.0 Hz. These findings are summarised in Tables A.2–A.5, where values fixed during the fitting process are indicated with square brackets. We provide all the parameters of both coronas for all the observations in Tables A.2–A.5.

4. Discussion

We analyse NICER observations of Swift J1727.8–1613 during the hard and hard-intermediate states of its first outburst, covering the period from MJD 60181 to 60226 (late August to mid-October 2023). The source shows type-C QPOs with centroid frequencies between 0.3 to 7.0 Hz. We model the time-averaged spectra of the source, as well as the RMS and phase-lag spectra of the QPO, using the time-dependent Comptonization model

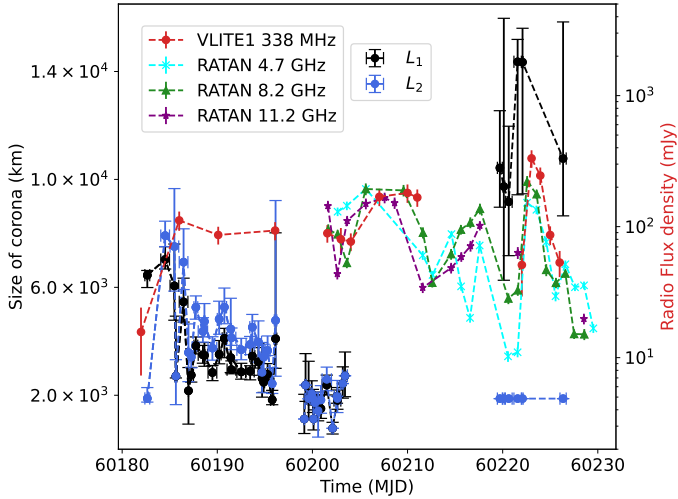


Fig. 8. Evolution of the sizes of the coronas, L_1 and L_2 , for Swift J1727.8–1613 using the `vkualdk` model. The right y axis shows the radio flux density in mJy obtained from the VLA Low-band Ionosphere and Transient Experiment (VLITE) at 338 MHz (red data points), data from Peters et al. (2023), alongside RATAN-600 observations at frequencies of 4.7 GHz (cyan data points), 8.2 GHz (green data points), and 11.2 GHz (purple data points, data from Ingram et al. 2024).

`vkompth`. At the start of the observations, approximately 90% of the total 2–20 keV flux comes from the corona and 5% comes from the disk, while by the end of the observations, the contribution of the corona and disk are 75% and 20%, respectively (see rows 6 and 10 of Table A.5). Our results indicate the presence of two horizontally extended coronas (C_1 and C_2 from now on) covering a truncated accretion disk. As the source progresses towards the HIMS, the inner disc moves closer to the black hole. Initially, C_1 and C_2 contract; later, C_1 expands. The temperature of the seed-photon source for both coronae increases from 0.3 keV to 0.7 keV, suggesting the corona shifts inwards along with the disk. In an alternative scenario, the corona remains around $10 R_g$ from the black hole while the disc moves inwards, such that seed photons that illuminate come progressively from regions of the disc closer to the black hole. We discuss the evolution of the corona and other spectral parameters in the context of radio observations in Section 4.2.

The power-law index, Γ , reaches a value of ~ 3 by the end of these observations. While $\Gamma \geq 2.5$ is typically associated with the soft-intermediate and soft states, the occurrence of Type-C QPOs, the slope of the power spectrum, the high amplitude of the broadband noise component, and the dominance of the non-thermal flux (comprising 80% of the total flux) indicate that in all these observations the source is in the hard-intermediate state. Furthermore, using the Power colour-colour diagram, and following the methodology outlined by Heil et al. (2015), Ingram et al. (2024) classified these observations as being in the hard-intermediate state, as shown in Figure 7 of their paper. Additionally, a photon index of $\Gamma \sim 2.9$ has been reported previously for the hard-intermediate state in the black hole binary GRS 1915+105 (Droulans & Jourdain 2009).

4.1. QPO lag spectrum: Evidence for a hard-to-soft lag transition

At lower QPO frequencies, $\nu_{\text{QPO}} \sim 0.3$ Hz, the lag spectrum displays a hard lag, where the 2.0–10 keV photons lag behind the 0.5–2.0 keV band photons by approximately 0.3 rad, or 150 ms.

For QPO frequencies in the range $0.8 \text{ Hz} < \nu_{\text{QPO}} \leq 1.2$ Hz, the lag spectrum gradually flattens, with the lags fluctuating at around -0.1 rad and $+0.1$ rad. Here, the time lag between the 2.0–10 keV and 0.5–2.0 keV bands decreases progressively from about 15 ms down to 2 ms. As the QPO frequency exceeds 1.2 Hz, the lag spectrum transitions to a soft lag, where the 0.5–2.0 keV photons lag behind the 2.0–10 keV photons. In this regime, the lag values shift to negative -1 ms at 1.2 Hz to -8 ms at 2.6 Hz, and further decrease, reaching values between -10 ms and -12 ms for frequencies in the range $6.2 \text{ Hz} < \nu_{\text{QPO}} < 7.0$ Hz. A similar transition of the QPO lag spectra from hard to soft as a function of QPO frequency has been previously observed in other black hole X-ray binaries, such as GRS 1915+105, around a QPO frequency of 2 Hz (see Figure 2 of Reig et al. 2000 and Figure 4 of Zhang et al. 2020) and for MAXI J1535–571 at a QPO frequency of 2.2 Hz (Garg et al. 2022).

The QPO fractional RMS amplitude increases from 7.6% to 9.3% as the QPO frequency increase from 0.34 Hz to 0.8 Hz. The sizes of the coronas are $L_1 \approx 6.5 \times 10^3$ km and $L_2 \approx 2 \times 10^3$ km. As the QPO frequency increases further from 0.8 Hz to 2.6 Hz, the QPO fractional RMS amplitude decreases from 9.3% to 6.1%. Both coronas shrink to $\sim 2 \times 10^3$ km at this point. For a QPO frequency in the range 6–7 Hz the fractional RMS amplitude further decreases from 2% to 1%; in this regime the two coronas separate themselves with C_1 expands from $\sim 2 \times 10^3$ km to $\sim 10^4$ km and we assumed that the C_2 remains of the size $\sim 2 \times 10^3$ km. From the model fits, η_{int} for both coronas is initially around 1–2% and then stays at 5% for both. A η_{int} of 5% suggests a horizontally extended corona, as a vertically extended corona would result in a much lower η_{int} (García et al. 2022). By the end of the observation, η_{int} increases to 15–20% for C_1 and 10% for C_2 , indicating that while the two coronas remain separated, they are still horizontally extended. In the LHS/HIMS of MAXI J1820+070, Ma et al. (2023) found that the two coronas gives similar values η_{int} (see Figure 9 of Ma et al. 2023) and explained it through horizontally extended coronas. The phase lag between the two coronas, ϕ , remains consistently close to π rad (see ϕ in Appendix Table A.2, A.3, A.4 and A.5). We note that ϕ is defined cyclically in the range $(-\pi, \pi)$. The fact that the two coronas are in anti-phase suggests that the time variations in the external heating rate –explicitly included in `vkompth`– and hence the energy, are transferred from one corona to the other over the course of the QPO cycle. Remarkably, this behaviour persists even as the QPO frequency changes by a factor of ~ 20 , pointing to a robust mechanism that couples the two regions over a wide range of timescales.

4.2. Dual corona

Our spectral-timing results indicate that on MJD 60181, as the X-ray flux increases (see Figure 1), $L_1 \approx 6.5 \times 10^3$ km and $L_2 \approx 2 \times 10^3$ km, while the inner disc is truncated at $\sim 40 R_g$. The seed-photon temperature for C_1 is always lower than C_2 . The intrinsic feedback fraction of 2% for both coronas implies that both coronas are horizontally extended and covering (part of) the accretion disk. During the same period, on MJD 60181.98, radio observations with the Very Large Array (VLA) at 5.25 and 7.45 GHz frequencies, shows that the source has an inverted spectral index ($S_\nu \propto \nu^\alpha$, with $\alpha = 0.2$), which implies the presence of a compact jet in the hard state (Miller-Jones et al. 2023b).

By MJD 60184, the disc moves closer to the black hole to $\sim 30 R_g$, the seed-photon temperatures for C_1 and C_2 increase to ~ 0.34 keV and 0.30 keV, respectively and both coronas expands to $\sim 7 \times 10^3$ km. The VLITE observations centred at MJD 60185.99

show a significant radio brightening (see left panel of Figure 1), confirmed by the Allen Telescope Array (Bright et al. 2023). The inner disc radius moves to $\sim 25 R_g$ and both coronas shrink further to $\sim 3 \times 10^3$ km. The seed-photon temperature of C_1 is always lower than that of C_2 (see Table A.2). From MJD 60186.08–60193.94 an extended continuous jet, which became fainter and less extended while the core brightness remained relatively constant, has been reported (Wood et al. 2024). The sudden increase in the seed-photon temperature of C_1 could be associated with a discrete southern jet knot (Wood et al. 2024), which occurs at nearly the same time. Wood et al. (2024) propose that this knot may arise from downstream internal shocks or jet-interstellar medium interactions over transient relativistic jets. A comprehensive investigation into the impact of these shocks on the disk-corona system would require detailed radio and X-ray simulations, which is beyond the scope of this study.

Between MJD 60199 and MJD 60201, the QPO frequency, inner disc temperature, seed-photon temperature, power-law index, and inner disc radius all exhibit abrupt increases followed by declines. This marks the transition of the source to a softer state before it fully transitioned to the high-soft state. At MJD 60202 the inner disc radius decreases to $\sim 10 R_g$, while the corona size remains more or less constant at nearly $\sim 2 \times 10^3$ km. The seed-photon temperature for C_1 is ~ 0.3 keV and the seed-photon temperature for C_2 is ~ 0.45 keV, which marks the separation of both coronas, although the sizes are nearly the same. Using ART-XC observations, Mereminskiy et al. (2024) reported a transition from a type-C into type-B QPO at MJD 60205 just before a giant X-ray flare reported by MAXI at MJD 60206.5 followed by a radio flare peak at MJD 60209.99 (see Figure 1). Since NICER did not observe the source during this period, we are unable to determine any changes in coronal properties during this period.

Between MJD 60219 and MJD 60222, the inner disc radii remains at $\sim 5 R_g$, C_1 expands again reaching a size of nearly $\sim 10^4$ km and C_2 being at the $\sim 2 \times 10^3$ km (we fix it as we could not constrain it.). The intrinsic feedback fraction of C_1 increases to $\sim 20\%$ while that of C_2 is $\sim 10\%$. A second radio flare, observed by the VLA at 5.25 GHz, shows a rapid increase of the compact jet flux density, from 7.2 ± 0.1 mJy to 235.8 ± 1.1 mJy within a day (MJD 60222–60223; Miller-Jones et al. 2023a). The quenching of the compact radio jet, and the subsequent dramatic radio flare with flattening of the spectral index, strongly suggest the ejection of transient, relativistic jets (Fender et al. 2004). Through X-ray hardness and intensity with MAXI, Mata Sánchez et al. (2024) claimed that the source made short transitions to the soft-intermediate state during the same period. If these state transitions are indeed linked to jet ejections, then the Comptonizing medium could serve as the source of the ejected material as proposed by Rodriguez et al. (2003) for the microquasar source XTE J1550–564 and by Méndez et al. (2022) for GRS 1915+105. Due to the lower significance of the QPO in this period, we are unable to assess whether there are changes in the coronal or disc properties associated with the radio flare or the transition to the soft-intermediate state in this work.

Later, on 14 October (MJD 60231.540) a bright flare was detected with the RATAN-600 radio telescope with a flux of 770 ± 30 mJy at 11.2 GHz (Trushkin et al. 2023), which could potentially signify that the source transitioned to the SIMS (Fender et al. 2004). Our results show that before transitioning to the SIMS, the size of corona 1 expands from $\sim 2 \times 10^3$ km to $\sim 10^4$ km. A similar horizontal expansion in the coronal size, staying parallel to the accretion disk, was reported by Ma et al.

(2023) for the BHXB source MAXI J1820+070 in the HIMS using the *vkompth* model (see Figure 11 of Ma et al. 2023). It should be noted that the *vkompth* model assumes a spherical coronal geometry; however, the true coronal geometry may be more complex. Therefore, the corona size reported here should be interpreted as a characteristic size rather than the exact physical size (see Méndez et al. 2022; García et al. 2022).

For a horizontally extended corona, the expected PA is aligned with the jet axis (Poutanen & Svensson 1996; Ursini et al. 2022). Assuming the radio polarization aligns with the jet direction, Ingram et al. (2024) reported that the radio polarization is consistent with the X-ray PA ($\sim 2^\circ$) for Swift J1727. The alignment of the PA with the radio jet direction also indicates that the corona is horizontally extended. Our proposed geometry of the corona is consistent with the polarimetry results obtained with IXPE (Ingram et al. 2024) for Swift J1727. The seed-photon temperature of the two coronas differs, with C_1 consistently having a lower seed-photon temperature than C_2 . This suggests that C_1 covers the outer parts of the disk, while C_2 covers the inner regions, with some overlap, as their temperatures differ by 100 eV only. Here, C_1 primarily influences the RMS and lag spectra at the QPO frequency, while C_2 dominates the time-averaged spectrum. The fact that the two coronal temperatures were required to reproduce the observed phase lag spectra suggests that the two coronas overlap.

Acknowledgements. We thank the referee for their constructive suggestions and comments which has improved the quality of the manuscript. This research has made use of NICER data and HEASOFT software provided by the High Energy Astrophysics Science Archive Research Center (HEASARC), which is a service of the Astrophysics Science Division at NASA/GSFC. DR acknowledges financial support from Centre National d'Études Spatiales (CNES) and the Science Survey Center of XMM-Newton. MM acknowledges support from the research programme Athena with project number 184.034.002, which is (partly) financed by the Dutch Research Council (NWO). FG is a CONICET Researcher. FG acknowledges support from PIP 0113 and PIBAA 1275 (CONICET).

References

- Alabarta, K., Méndez, M., García, F., et al. 2025, *ApJ*, **980**, 251
 Basko, M. M., Sunyaev, R. A., & Titarchuk, L. G. 1974, *A&A*, **31**, 249
 Bellavita, C., García, F., Méndez, M., & Karpouzas, K. 2022, *MNRAS*, **515**, 2099
 Belloni, T., & Hasinger, G. 1990, *A&A*, **230**, 103
 Belloni, T., Psaltis, D., & van der Klis, M. 2002, *ApJ*, **572**, 392
 Belloni, T., Homan, J., Casella, P., et al. 2005, *A&A*, **440**, 207
 Belloni, T. M., Motta, S. E., & Muñoz-Darias, T. 2011, *Bull. Astron. Soc. India*, **39**, 409
 Bhargava, Y., Belloni, T., Bhattacharya, D., Motta, S., & Ponti, G. 2021, *MNRAS*, **508**, 3104
 Bouchet, T., Rodriguez, J., Cangemi, F., et al. 2024, *A&A*, **688**, L5
 Bright, J., Farah, W., Fender, R., et al. 2023, *ATel*, **16228**, 1
 Cabanac, C., Henri, G., Petrucci, P. O., et al. 2010, *MNRAS*, **404**, 738
 Cadolle Bel, M., Sizon, P., Goldwurm, A., et al. 2006, *A&A*, **446**, 591
 Casella, P., Belloni, T., Homan, J., & Stella, L. 2004, *A&A*, **426**, 587
 Chen, X., Swank, J. H., & Taam, R. E. 1997, *ApJ*, **477**, L41
 Done, C., Gierliński, M., & Kubota, A. 2007, *A&ARv*, **15**, 1
 Droulans, R., & Jourdain, E. 2009, *A&A*, **494**, 229
 Fender, R. P., Belloni, T. M., & Gallo, E. 2004, *MNRAS*, **355**, 1105
 García, F., Méndez, M., Karpouzas, K., et al. 2021, *MNRAS*, **501**, 3173
 García, F., Karpouzas, K., Méndez, M., et al. 2022, *MNRAS*, **513**, 4196
 Garg, A., Misra, R., & Sen, S. 2022, *MNRAS*, **514**, 3285
 Gendreau, K. C., Arzoumanian, Z., Adkins, P. W., et al. 2016, *SPIE Conf. Ser.*, **9905**, 99051H
 Gierliński, M., Zdziarski, A. A., Done, C., et al. 1997, *MNRAS*, **288**, 958
 Gilfanov, M. 2010, in *Lecture Notes in Physics*, eds. T. Belloni (Berlin Heidelberg: Springer), 17
 Hameury, J. M., Lasota, J. P., McClintock, J. E., & Narayan, R. 1997, *ApJ*, **489**, 234
 Heil, L. M., Uttley, P., & Klein-Wolt, M. 2015, *MNRAS*, **448**, 3339
 Homan, J., Wijnands, R., van der Klis, M., et al. 2001, *ApJS*, **132**, 377

- Ingram, A. R., & Motta, S. E. 2019, *New Astron. Rev.*, **85**, 101524
- Ingram, A., Bollemeijer, N., Veledina, A., et al. 2024, *ApJ*, **968**, 76
- Karpouzas, K., Méndez, M., Ribeiro, E. M., et al. 2020, *MNRAS*, **492**, 1399
- Kubota, A., Tanaka, Y., Makishima, K., et al. 1998, *PASJ*, **50**, 667
- Kumar, N., & Misra, R. 2014, *MNRAS*, **445**, 2818
- Lee, H. C., & Miller, G. S. 1998, *MNRAS*, **299**, 479
- Lee, H. C., Misra, R., & Taam, R. E. 2001, *ApJ*, **549**, L229
- Lense, J., & Thirring, H. 1918, *Phys. Zeitschr.*, **19**, 156
- Liao, J., Chang, N., Cui, L., et al. 2024, ArXiv e-prints [arXiv:2410.06574]
- Liu, H., Ji, L., Bambi, C., et al. 2021, *ApJ*, **909**, 63
- Ma, R., Méndez, M., García, F., et al. 2023, *MNRAS*, **525**, 854
- Magdziarz, P., & Zdziarski, A. A. 1995, *MNRAS*, **273**, 837
- Makishima, K., Maejima, Y., Mitsuda, K., et al. 1986, *ApJ*, **308**, 635
- Mastichiadis, A., Petropoulou, M., & Kylafis, N. D. 2022, *A&A*, **662**, A118
- Mata Sánchez, D., Muñoz-Darias, T., Armas Padilla, M., Casares, J., & Torres, M. A. P. 2024, *A&A*, **682**, L1
- Méndez, M., & van der Klis, M. 1997, *ApJ*, **479**, 926
- Méndez, M., Karpouzas, K., García, F., et al. 2022, *Nat. Astron.*, **6**, 577
- Méndez, M., Peirano, V., García, F., et al. 2024, *MNRAS*, **527**, 9405
- Mereminskiy, I., Lutovinov, A., Molkov, S., et al. 2024, *MNRAS*, **531**, 4893
- Miller-Jones, J. C. A., Bahramian, A., Altamirano, D., et al. 2023a, *ATel*, **16271**, 1
- Miller-Jones, J. C. A., Sivakoff, G. R., Bahramian, A., & Russell, T. D. 2023b, *ATel*, **16211**, 1
- Misra, R., Rawat, D., Yadav, J. S., & Jain, P. 2020, *ApJ*, **889**, L36
- Mitsuda, K., Inoue, H., Koyama, K., et al. 1984, *PASJ*, **36**, 741
- Motta, S., Homan, J., Muñoz Darias, T., et al. 2012, *MNRAS*, **427**, 595
- Motta, S. E., Belloni, T. M., Stella, L., Muñoz-Darias, T., & Fender, R. 2014a, *MNRAS*, **437**, 2554
- Motta, S. E., Muñoz-Darias, T., Sanna, A., et al. 2014b, *MNRAS*, **439**, L65
- Motta, S. E., Casella, P., Henze, M., et al. 2015, *MNRAS*, **447**, 2059
- Nandi, A., Das, S., Majumder, S., et al. 2024, *MNRAS*, **531**, 1149
- Negoro, H., Serino, M., Nakajima, M., et al. 2023, *ATel*, **16205**, 1
- Nowak, M. A. 2000, *MNRAS*, **318**, 361
- O'Connor, B., Hare, J., Younes, G., et al. 2023, *ATel*, **16207**, 1
- O'Neill, S. M., Reynolds, C. S., Miller, M. C., & Sorathia, K. A. 2011, *ApJ*, **736**, 107
- Page, K. L., Dichiara, S., Gropp, J. D., et al. 2023, *GRB Coordinates Network*, **34537**, 1
- Peters, W. M., Polisenky, E., Clarke, T. E., Giacintucci, S., & Kassim, N. E. 2023, *ATel*, **16279**, 1
- Podgorný, J., Svoboda, J., Dovčiak, M., et al. 2024, *A&A*, **686**, L12
- Poutanen, J., & Svensson, R. 1996, *ApJ*, **470**, 249
- Psaltis, D., Belloni, T., & van der Klis, M. 1999, *ApJ*, **520**, 262
- Rawat, D., Husain, N., & Misra, R. 2023a, *MNRAS*, **524**, 5869
- Rawat, D., Méndez, M., García, F., et al. 2023b, *MNRAS*, **520**, 113
- Reig, P., Belloni, T., van der Klis, M., et al. 2000, *ApJ*, **541**, 883
- Remillard, R. A., & McClintock, J. E. 2006, *ARA&A*, **44**, 49
- Remillard, R. A., Sobczak, G. J., Muno, M. P., & McClintock, J. E. 2002, *ApJ*, **564**, 962
- Reynolds, C. S., & Fabian, A. C. 2008, *ApJ*, **675**, 1048
- Rodriguez, J., Corbel, S., & Tomsick, J. A. 2003, *ApJ*, **595**, 1032
- Rout, S. K., Méndez, M., & García, F. 2023, *MNRAS*, **525**, 221
- Shakura, N. I., & Sunyaev, R. A. 1973, *A&A*, **24**, 337
- Shimura, T., & Takahara, F. 1995, *ApJ*, **445**, 780
- Stella, L., & Vietri, M. 1998, *ApJ*, **492**, L59
- Stella, L., Vietri, M., & Morsink, S. M. 1999, *ApJ*, **524**, L63
- Tagger, M., & Pellat, R. 1999, *A&A*, **349**, 1003
- Takizawa, M., Dotani, T., Mitsuda, K., et al. 1997, *ApJ*, **489**, 272
- Titarchuk, L., & Fiorito, R. 2004, *ApJ*, **612**, 988
- Trushkin, S. A., Bursov, N. N., Nizhelskij, N. A., & Tsybulev, P. G. 2023, *ATel*, **16289**, 1
- Ursini, F., Matt, G., Bianchi, S., et al. 2022, *MNRAS*, **510**, 3674
- van der Klis, M., & Jansen, F. A. 1985, *Nature*, **313**, 768
- Veledina, A., Muleri, F., Dovčiak, M., et al. 2023, *ApJ*, **958**, L16
- Verner, D. A., Ferland, G. J., Korista, K. T., & Yakovlev, D. G. 1996, *ApJ*, **465**, 487
- Wijnands, R., Homan, J., & van der Klis, M. 1999, *ApJ*, **526**, L33
- Wilms, J., Allen, A., & McCray, R. 2000, *ApJ*, **542**, 914
- Wood, C. M., Miller-Jones, J. C. A., Bahramian, A., et al. 2024, *ApJ*, **971**, L9
- Zdziarski, A. A., Johnson, W. N., & Magdziarz, P. 1996, *MNRAS*, **283**, 193
- Zhang, L., Méndez, M., Altamirano, D., et al. 2020, *MNRAS*, **494**, 1375
- Zhang, Y., Méndez, M., García, F., et al. 2022, *MNRAS*, **512**, 2686
- Zhang, L., Méndez, M., García, F., et al. 2023b, *MNRAS*, **526**, 3944
- Zhang, Y., Méndez, M., García, F., et al. 2023a, *MNRAS*, **520**, 5144
- Zhang, Z., Liu, H., Rawat, D., et al. 2024, *ApJ*, **971**, 148
- Życki, P. T., Done, C., & Smith, D. A. 1999, *MNRAS*, **309**, 561

Appendix A: Figures and tables

We show NICER observations details in Table A.1, which lists the observation number, NICER OBSID, mid-time MJD, and exposure in kiloseconds. We present the fit to the PDS and the real and imaginary components of the cross spectrum for OBSID 6557020402 in Figure A.1. The panels are similar to the Figure 3. Figure A.2 displays the time-averaged spectrum of the source fitted with the model TBfe0*(diskbb + nthComp) (top panel), along with the RMS and phase-lag spectra of the 7.0 Hz QPO, fitted with the models vkompthdk*dilution and vkompthdk, respectively (middle and bottom panels). The vkompthdk model is shown in blue. The solid red line in middle and bottom panels represent the best fit model of vkdualdk*dilution and vkdualdk to, respectively, the RMS and phase-lag spectra of the QPO.

Figure A.3 shows corner plot of the parameters for Swift J1727 in ObsID 6203980105, fitted with the vkdualdk model. The contours represent the 1σ , 2σ , and 3σ confidence levels for pairs of parameters, while the vertical lines indicate the 1σ confidence intervals for individual parameters. Tables A.2, A.3, A.4 and A.5 give the time-averaged spectral and corona model parameters of Swift J1727 for observations 1 to 54. The rows include the observation number, QPO frequency, time lag of the QPO between the 0.5–2.0 keV and 2.0–10.0 keV bands, hydrogen column density (N_{H}), power-law photon index of NTHCOMP (Γ), inner disc temperature (kT_{in}), seed photon temperature of VKDUALDK ($kT_{\text{s},1}$), sizes of the two coronae (L_1 and L_2), fraction of flux from the seed photon source due to feedback from the corona (η_1 and η_2), as well as the chi-square and degrees of freedom of the fit. Errors are given at 1σ confidence levels.

Table A.1. NICER observation log of Swift J1727.8–1613.

Obs	ObsID	Time (MJD mean)	t_{exp} (ks)	count rate (10^2 counts s^{-1})	QPO frequency (Hz)	QPO Fractional RMS (%)
1	*6203980101	60181.38	0.5	153.3 ± 0.8	0.357 ± 0.011	2.9*
2	6203980102	60182.64	1.1	492.9 ± 0.1	0.334 ± 0.003	7.6 ± 0.3
3	6203980103	60183.38	0.5	550.1 ± 0.3	0.454 ± 0.006	8.0 ± 0.8
4	6203980103	60183.59	0.5	618.4 ± 0.3	0.604 ± 0.004	8.8 ± 0.4
5	6203980104	60184.52	3.1	732.1 ± 0.1	0.788 ± 0.003	9.3 ± 0.2
6	6203980105	60185.49	3.8	747.5 ± 0.1	0.887 ± 0.002	8.9 ± 0.1
7	6703010101	60185.65	3.4	741.1 ± 0.1	0.867 ± 0.003	9.2 ± 0.2
8	6203980106	60186.46	10.6	783.9 ± 0.1	1.111 ± 0.002	8.6 ± 0.1
9	6750010101	60186.97	0.6	783.0 ± 0.2	1.187 ± 0.004	8.4 ± 0.3
10	6750010102	60187.26	7.4	775.8 ± 0.1	1.123 ± 0.002	8.3 ± 0.1
11	6203980107	60187.75	5.4	770.8 ± 0.1	1.189 ± 0.003	8.0 ± 0.2
12	6203980108	60188.49	9.4	771.1 ± 0.1	1.239 ± 0.002	8.2 ± 0.1
13	6703010102	60188.65	3.7	767.0 ± 0.1	1.216 ± 0.002	8.5 ± 0.2
14	6203980109	60189.49	12.6	755.7 ± 0.1	1.261 ± 0.001	8.5 ± 0.1
15	6750010201	60190.20	7.2	756.2 ± 0.1	1.307 ± 0.002	8.2 ± 0.1
16	6203980110	60190.75	6.7	746.8 ± 0.1	1.304 ± 0.002	8.0 ± 0.1
17	6203980111	60191.49	9.8	703.1 ± 0.1	1.178 ± 0.001	8.3 ± 0.1
18	6703010103	60191.42	2.8	699.2 ± 0.1	1.127 ± 0.004	8.1 ± 0.3
19	6203980112	60192.52	6.8	707.7 ± 0.1	1.424 ± 0.002	7.3 ± 0.1
20	6750010301	60193.46	7.3	708.0 ± 0.1	1.427 ± 0.002	8.0 ± 0.1
21	6203980113	60193.68	5.4	701.5 ± 0.1	1.398 ± 0.002	7.6 ± 0.1
22	6203980114	60194.32	7.4	693.2 ± 0.1	1.478 ± 0.010	6.2 ± 0.3
23	6703010104	60194.71	0.8	714.0 ± 0.2	1.622 ± 0.006	7.4 ± 0.2
24	6750010501	60194.87	2.3	682.7 ± 0.1	1.448 ± 0.004	8.0 ± 0.1
25	6750010502	60195.29	4.8	661.6 ± 0.1	1.358 ± 0.002	7.9 ± 0.1
26	6203980115	60195.77	1.3	647.4 ± 0.2	1.352 ± 0.005	7.3 ± 0.2
27	6203980116	60196.13	0.5	648.0 ± 0.2	1.397 ± 0.010	7.0 ± 0.3
28	6703010106	60199.15	0.2	685.1 ± 0.2	2.267 ± 0.010	5.9 ± 0.3
29	6703010106	60199.28	0.4	737.5 ± 0.2	2.760 ± 0.008	5.5 ± 0.2
30	6203980118	60199.60	0.8	705.1 ± 0.2	2.455 ± 0.008	5.7 ± 0.2
31	6203980118	60199.93	1.1	775.7 ± 0.2	3.154 ± 0.007	5.4 ± 0.1
32	6511080101	60200.06	0.6	793.2 ± 0.3	3.378 ± 0.008	5.0 ± 0.1
33	6511080101	60200.12	0.6	735.2 ± 0.3	2.827 ± 0.008	5.3 ± 0.1
34	6203980119	60200.28	2.1	723.5 ± 0.1	2.704 ± 0.005	5.7 ± 0.1
35	6203980119	60200.60	1.4	688.1 ± 0.1	2.606 ± 0.004	5.7 ± 0.1
36	6203980119	60200.90	1.3	628.7 ± 0.1	2.056 ± 0.004	6.3 ± 0.1
37	6203980120	60201.51	6.3	607.6 ± 0.1	1.992 ± 0.003	6.3 ± 0.1
38	6203980121	60202.12	1.7	636.8 ± 0.2	2.308 ± 0.004	5.7 ± 0.1
39	6703010107	60202.63	4.5	678.9 ± 0.1	2.555 ± 0.004	6.1 ± 0.1
40	6750010202	60202.58	6.5	669.2 ± 0.1	2.740 ± 0.003	5.5 ± 0.1
41	6750010203	60203.19	1.9	641.7 ± 0.2	2.480 ± 0.004	5.7 ± 0.1
42	6203980122	60203.43	1.0	686.6 ± 0.2	2.531 ± 0.012	5.2 ± 0.2
43	6203980130	60219.70	2.6	666.9 ± 0.1	6.195 ± 0.022	2.1 ± 0.1
44	6203980131	60220.12	0.8	680.2 ± 0.2	6.856 ± 0.031	1.7 ± 0.1
45	6703010113	60220.64	3.5	677.2 ± 0.1	6.913 ± 0.021	1.6 ± 0.1
46	6557020401	60221.57	6.5	663.2 ± 0.1	6.840 ± 0.014	1.6 ± 0.1
47	6557020402	60222.09	0.6	652.5 ± 0.2	7.067 ± 0.032	1.5 ± 0.1
48	*6703010115	60222.54	1.3	707.8 ± 0.2	7.157 ± 0.175	0.7*
49	*6203980132	60222.67	2.3	714.9 ± 0.1	8.207 ± 0.241	0.4*
50	*6203980133	60223.51	5.2	697.1 ± 0.1	[8.2] ^f	0.2*
51	*6203980134	60224.51	3.9	679.0 ± 0.1	8.179 ± 0.209	0.3*
52	*6203980135	60225.54	0.6	663.8 ± 0.2	[8.2] ^f	0.3*
53	*6703010116	60225.45	3.1	666.0 ± 0.1	[8.2] ^f	0.1*
54	6203980136	60226.35	2.0	577.6 ± 0.1	6.697 ± 0.027	1.1 ± 0.1

Notes. The columns list the observation number, NICER ObsID, mid-time MJD, exposure in kilo seconds, t_{exp} , the 0.5–10.0 keV count rate, the QPO frequency and QPO fractional RMS amplitude. All uncertainties are provided at the 1σ confidence level. *Observations with QPO's significance less than 3σ . ^f3- σ upper limit of the parameter. ^afixed parameter during the fitting.

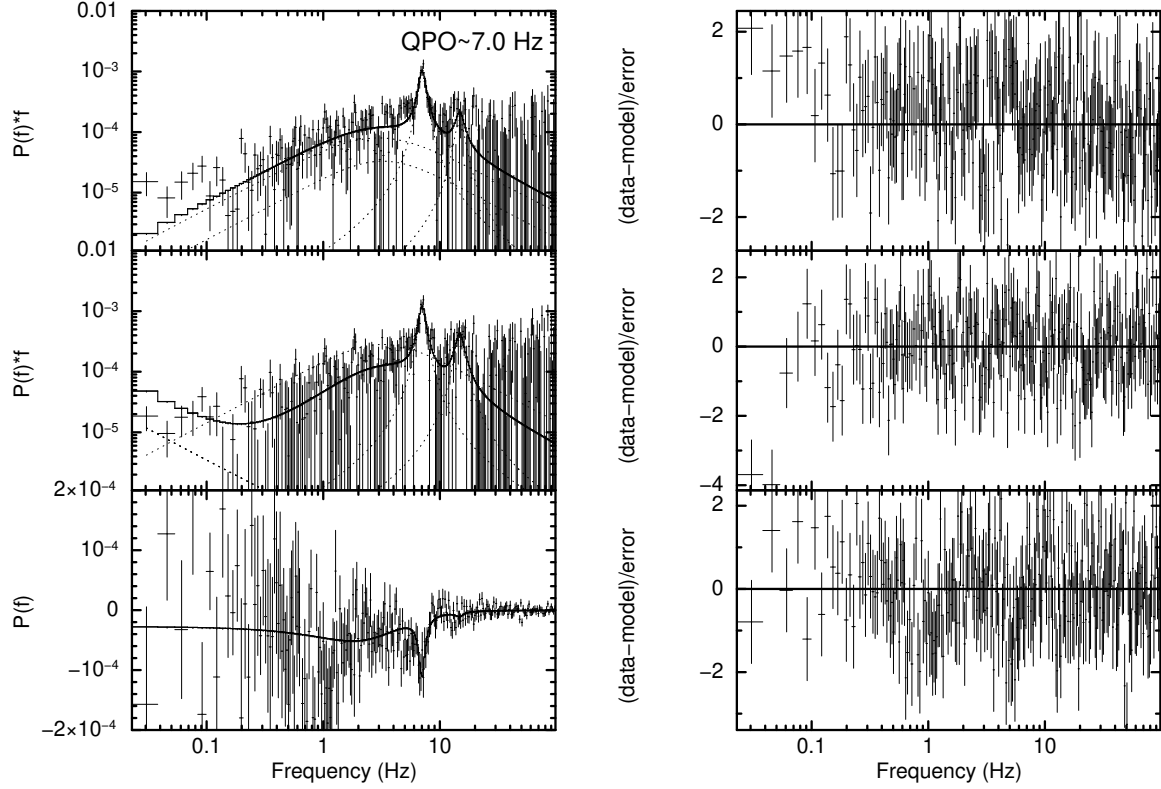


Fig. A.1. Same as Figure 3 but for observation ID 6557020402 when the type-C QPO centroid frequency was 7.0 Hz.

Table A.2. Time-averaged spectral and corona model parameters of Swift J1727.8–1613.

		Observation number											
Component	Parameter	2	5	6	7	8	9	10	11	12	13	14	
	QPO frequency (Hz)	0.334 ± 0.003	0.788 ± 0.003	0.887 ± 0.002	0.867 ± 0.003	1.111 ± 0.002	1.187 ± 0.004	1.123 ± 0.002	1.189 ± 0.003	1.239 ± 0.002	1.216 ± 0.002	1.261 ± 0.001	
	time lag (10^{-2} sec)	15.49 ± 2.0	2.12 ± 0.27	2.12 ± 0.19	1.55 ± 0.18	0.31 ± 0.08	-0.14 ± 0.2	0.26 ± 0.1	0.46 ± 0.1	-0.03 ± 0.06	-0.06 ± 0.08	-0.13 ± 0.04	
TBfeo	N_{H} (10^{22} cm $^{-2}$)	$[0.28]^a$	$[0.28]^a$	$[0.28]^a$	$[0.28]^a$	$[0.28]^a$	$[0.28]^a$	$[0.28]^a$	$[0.28]^a$	$[0.28]^a$	$[0.28]^a$	$[0.28]^a$	
diskbb	kT_{in} (keV)	0.270 ± 0.001	0.339 ± 0.003	0.352 ± 0.003	0.350 ± 0.001	0.376 ± 0.003	0.396 ± 0.004	0.389 ± 0.004	0.386 ± 0.003	0.389 ± 0.003	0.388 ± 0.003	0.393 ± 0.003	
	N_{disk}^b (10^4)	31.7 ± 1.0	17.8 ± 0.4	15.7 ± 0.4	15.9 ± 0.2	12.1 ± 0.2	10.3 ± 0.2	10.6 ± 0.2	10.9 ± 0.2	10.3 ± 0.2	10.5 ± 0.2	9.9 ± 0.2	
	F_{disk}^c (10^{-8} ergs cm $^{-2}$ s $^{-1}$)	3.4 ± 0.1	4.8 ± 0.1	4.8 ± 0.1	4.8 ± 0.1	5.0 ± 0.1	5.2 ± 0.1	5.0 ± 0.0	5.0 ± 0.1	4.8 ± 0.1	4.9 ± 0.1	4.9 ± 0.1	
nthComp	Γ	1.621 ± 0.005	1.721 ± 0.006	1.742 ± 0.003	1.735 ± 0.005	1.799 ± 0.003	1.817 ± 0.011	1.803 ± 0.003	1.812 ± 0.004	1.835 ± 0.004	1.828 ± 0.003	1.832 ± 0.003	
	kT_e (keV)	$[40]^a$	$[40]^a$	$[40]^a$	$[40]^a$	$[40]^a$	$[40]^a$	$[40]^a$	$[40]^a$	$[40]^a$	$[40]^a$	$[40]^a$	
	N_{nthComp}	23.5 ± 0.1	33.6 ± 0.3	34.4 ± 0.3	33.9 ± 0.2	36.2 ± 0.3	35.5 ± 0.5	35.5 ± 0.3	35.6 ± 0.3	36.0 ± 0.3	35.5 ± 0.3	34.8 ± 0.3	
	F_{nthComp}^c (10^{-8} ergs cm $^{-2}$ s $^{-1}$)	56.7 ± 0.7	62.6 ± 0.6	60.9 ± 0.2	61.3 ± 0.5	56.7 ± 0.2	54.3 ± 0.7	55.8 ± 0.1	54.5 ± 0.2	52.4 ± 0.2	52.5 ± 0.1	51.3 ± 0.1	
gaussian	$lineE$ (keV)	$[6.4]^a$	$[6.4]^a$	$[6.4]^a$	$[6.4]^a$	$[6.4]^a$	$[6.4]^a$	$[6.4]^a$	$[6.4]^a$	$[6.4]^a$	$[6.4]^a$	$[6.4]^a$	
	σ (keV)	1.3 ± 0.1	1.1 ± 0.1	$[1.0]^a$	1.1 ± 0.1	$[1.0]^a$	1.0 ± 0.2	$[1.0]^a$	$[1.0]^a$	1.0 ± 0.1	$[1.0]^a$	$[1.0]^a$	
	Strength (10^{-1})	2.8 ± 0.4	2.9 ± 0.4	$[2.0]^a$	2.7 ± 0.4	$[2.0]^a$	2.0 ± 0.5	$[2.0]^a$	$[2.0]^a$	2.0 ± 0.2	$[2.0]^a$	$[2.0]^a$	
vkdualdk	$kT_{\text{S}1}$ (keV)	$0.248^{+0.003}_{-0.011}$	$0.299^{+0.032}_{-0.028}$	$0.286^{+0.020}_{-0.055}$	$0.325^{+0.002}_{-0.001}$	$0.301^{+0.021}_{-0.059}$	$0.267^{+0.055}_{-0.069}$	$0.292^{+0.016}_{-0.013}$	$0.301^{+0.128}_{-0.111}$	$0.294^{+0.018}_{-0.030}$	$0.276^{+0.031}_{-0.043}$	$0.240^{+0.014}_{-0.031}$	
	L_1 (10^3 km)	$6.5^{+0.2}_{-0.5}$	$7.0^{+0.5}_{-0.4}$	$6.1^{+1.5}_{-1.3}$	$2.7^{+2.2}_{-0.1}$	$5.5^{+0.9}_{-0.7}$	$2.2^{+0.9}_{-1.2}$	2.7 ± 0.3	3.8 ± 0.3	3.5 ± 0.3	$3.5^{+0.5}_{-0.4}$	2.8 ± 0.3	
	L_2 (10^3 km)	$1.9^{+0.4}_{-0.1}$	$7.9^{+0.5}_{-0.4}$	$7.5^{+2.1}_{-1.7}$	$2.7^{+0.6}_{-1.1}$	$6.9^{+1.2}_{-1.0}$	3.6 ± 1.1	$3.4^{+0.2}_{-0.4}$	5.3 ± 0.4	$4.4^{+0.5}_{-0.4}$	$4.7^{+0.7}_{-0.6}$	3.7 ± 0.4	
	η_1	0.17 ± 0.01	$0.27^{+0.01}_{-0.03}$	$0.28^{+0.02}_{-0.04}$	$0.28^{+0.02}_{-0.01}$	$0.28^{+0.01}_{-0.02}$	$0.27^{+0.03}_{-0.10}$	0.26 ± 0.01	$0.26^{+0.10}_{-0.04}$	$0.26^{+0.01}_{-0.02}$	$0.25^{+0.02}_{-0.03}$	$0.23^{+0.01}_{-0.03}$	
	η_2	0.19 ± 0.01	$0.29^{+0.01}_{-0.02}$	0.32 ± 0.01	$0.29^{+0.02}_{-0.03}$	$0.34^{+0.02}_{-0.01}$	$0.39^{+0.05}_{-0.03}$	0.33 ± 0.01	$0.32^{+0.10}_{-0.03}$	0.33 ± 0.01	$0.35^{+0.02}_{-0.01}$	$0.36^{+0.02}_{-0.01}$	
	$\delta\dot{H}_{\text{ext},1}$	$11.00^{+1.17}_{-1.53}$	$10.80^{+0.95}_{-1.29}$	$8.70^{+1.13}_{-1.35}$	$22.40^{+0.57}_{-2.31}$	$6.90^{+0.79}_{-0.85}$	$9.60^{+3.25}_{-18.87}$	$11.10^{+0.74}_{-1.48}$	$6.00^{+2.09}_{-2.43}$	$8.20^{+0.58}_{-0.71}$	$8.50^{+1.10}_{-2.09}$	$11.20^{+1.32}_{-3.32}$	
	$\delta\dot{H}_{\text{ext},2}$	$27.6^{+0.4}_{-1.17}$	$5.6^{+2.2}_{-0.7}$	$2.9^{+0.3}_{-0.7}$	$16.6^{+2.7}_{-2.1}$	$2.0^{+0.7}_{-2.1}$	$1.1^{+0.6}_{-0.5}$	$2.7^{+0.6}_{-0.2}$	$1.4^{+0.6}_{-0.2}$	$2.0^{+0.7}_{-0.4}$	$1.5^{+0.5}_{-0.9}$	1.1 ± 0.2	
	ϕ (rad)	$[-3]^a$	$3.10^{+0.01}_{-0.02}$	3.11 ± 0.01	$[-3]^a$	$-3.13^{+0.07}_{-0.01}$	$-3.03^{+0.17}_{-0.07}$	$3.14^{+0.04}_{-0.01}$	$3.12^{+0.04}_{-0.03}$	$-3.12^{+0.03}_{-0.01}$	$-3.08^{+0.06}_{-0.02}$	$-3.05^{+0.07}_{-0.04}$	
	$reflag$ (10^{-2})	29.4 ± 1.3	10.4 ± 0.7	8.2 ± 0.5	2.0 ± 1.9	4.3 ± 0.4	-0.4 ± 1.1	1.3 ± 0.6	5.5 ± 0.9	2.1 ± 0.4	1.5 ± 0.5	1.5 ± 0.3	
	$\eta_{\text{int},1}$	0.005 ± 0.001	0.019 ± 0.004	$0.014^{+0.003}_{-0.002}$	0.014 ± 0.001	$0.017^{+0.003}_{-0.002}$	$0.017^{+0.004}_{-0.002}$	0.016 ± 0.002	$0.018^{+0.009}_{-0.003}$	$0.017^{+0.002}_{-0.001}$	$0.016^{+0.001}_{-0.002}$	0.014 ± 0.001	
	$\eta_{\text{int},2}$	0.006 ± 0.001	$0.021^{+0.005}_{-0.004}$	0.017 ± 0.001	0.015 ± 0.001	$0.021^{+0.001}_{-0.003}$	$0.026^{+0.002}_{-0.003}$	0.021 ± 0.001	0.021 ± 0.005	0.023 ± 0.001	0.024 ± 0.001	0.025 ± 0.001	
	χ^2 (dof)	228.2 (241)	223.6 (248)	254.2 (251)	233.4 (242)	266.3 (251)	222.6 (229)	266.1 (251)	203.6 (242)	264.0 (249)	234.5 (248)	258.9 (254)	

Notes. The time lag is between the 0.5–2.0 keV and 2.0–10.0 keV band of the QPO. The reference lag, $reflag$, of the model is in the 0.5–10.0 keV energy band. The errors are at 1σ confidence levels. ^(a) Fixed parameter during the fitting. ^(b) Parameter tied during fitting. ^(c) Unabsorbed flux in the 0.5–10.0 keV energy band.

Table A.3. Same as Table A.2 for observation numbers 15 to 25.

Component	Parameter	Observation number										
		15	16	17	18	19	20	21	22	23	24	25
TBfeo	QPO frequency (Hz)	1.307 ± 0.002	1.304 ± 0.002	1.178 ± 0.001	1.127 ± 0.004	1.424 ± 0.002	1.427 ± 0.002	1.398 ± 0.002	1.478 ± 0.01	1.622 ± 0.006	1.448 ± 0.004	1.358 ± 0.002
	time lag (10^{-2} sec)	-0.18 ± 0.05	-0.13 ± 0.05	0.19 ± 0.04	0.42 ± 0.13	-0.66 ± 0.06	-0.41 ± 0.05	-0.33 ± 0.06	-0.32 ± 0.11	-0.67 ± 0.16	-0.15 ± 0.09	-0.17 ± 0.06
diskbb	N_{H} (10^{22} cm $^{-2}$)	[0.28] ^a	[0.28] ^a	[0.28] ^a	[0.28] ^a	[0.28] ^a	[0.28] ^a	[0.28] ^a	[0.28] ^a	[0.28] ^a	[0.28] ^a	
nthComp	kT_{in} (keV)	0.400 ± 0.003	0.397 ± 0.003	0.381 ± 0.003	0.377 ± 0.003	0.391 ± 0.003	0.402 ± 0.003	0.400 ± 0.002	0.397 ± 0.003	0.418 ± 0.004	0.399 ± 0.003	0.400 ± 0.003
	N_{disk}^b (10^4)	9.1 ± 0.2	9.4 ± 0.2	10.9 ± 0.2	11.3 ± 0.2	9.3 ± 0.2	8.6 ± 0.2	8.8 ± 0.1	8.8 ± 0.1	7.1 ± 0.1	8.4 ± 0.2	8.7 ± 0.2
gaussian	F_{disk}^* (10^{-8} ergs cm $^{-2}$ s $^{-1}$)	4.8 ± 0.1	4.8 ± 0.1	4.7 ± 0.1	4.7 ± 0.1	4.5 ± 0.1	4.6 ± 0.1	4.6 ± 0.1	4.5 ± 0.1	4.5 ± 0.1	4.4 ± 0.1	4.6 ± 0.1
	Γ	1.857 ± 0.003	1.845 ± 0.003	1.811 ± 0.003	1.803 ± 0.006	1.865 ± 0.003	1.874 ± 0.005	1.868 ± 0.004	1.878 ± 0.003	1.932 ± 0.006	1.894 ± 0.008	1.855 ± 0.005
vkdualdk	kT_e (keV)	[40] ^a	[40] ^a	[40] ^a	[40] ^a	[40] ^a	[40] ^a	[40] ^a	[40] ^a	[40] ^a	[40] ^a	
	N_{nthComp}	35.1 ± 0.3	34.4 ± 0.3	32.2 ± 0.2	32.0 ± 0.3	33.1 ± 0.3	32.6 ± 0.3	32.3 ± 0.2	32.3 ± 0.3	33.5 ± 0.4	32.0 ± 0.4	29.9 ± 0.3
gaussian	F_{nthComp}^* (10^{-8} ergs cm $^{-2}$ s $^{-1}$)	49.1 ± 0.1	49.4 ± 0.1	49.2 ± 0.1	49.6 ± 0.4	45.1 ± 0.1	44.2 ± 0.2	44.2 ± 0.2	42.9 ± 0.1	40.8 ± 0.2	41.5 ± 0.3	42.0 ± 0.3
	lineE (keV)	[6.4] ^a	[6.4] ^a	[6.4] ^a	[6.4] ^a	[6.4] ^a	[6.4] ^a	[6.4] ^a	[6.4] ^a	[6.4] ^a	[6.4] ^a	[6.4] ^a
vkdualdk	σ (keV)	[1.0] ^a	[1.0] ^a	[1.0] ^a	1.1 ± 0.1	[1.0] ^a	1.0 ± 0.1	1.0 ± 0.1	[1.0] ^a	[1.0] ^a	1.2 ± 0.2	1.0 ± 0.1
	Strength (10^{-1})	[2.0] ^a	[2.0] ^a	[2.0] ^a	2.2 ± 0.3	[2.0] ^a	1.4 ± 0.2	1.5 ± 0.2	[2.0] ^a	[2.0] ^a	1.9 ± 0.4	1.5 ± 0.2
vkdualdk	kT_{S_1} (keV)	0.290 ^{+0.029} _{-0.022}	0.306 ^{+0.018} _{-0.041}	0.263 ^{+0.023} _{-0.013}	0.271 ^{+0.029} _{-0.020}	0.262 ^{+0.012} _{-0.010}	0.303 ^{+0.016} _{-0.028}	0.296 ^{+0.025} _{-0.037}	0.319 ^{+0.052} _{-0.030}	0.273 ^{+0.073} _{-0.035}	0.268 ^{+0.033} _{-0.041}	0.281 ^{+0.033} _{-0.011}
	L_1 (10^3 km)	3.5 ^{+0.3} _{-0.4}	4.1 ^{+0.4} _{-0.7}	2.9 ^{+0.3} _{-0.2}	3.4 ± 0.6	2.9 ± 0.3	2.9 ^{+0.2} _{-0.3}	3.5 ^{+0.3} _{-0.4}	3.2 ^{+0.7} _{-0.5}	2.6 ^{+1.1} _{-0.7}	2.5 ± 0.4	2.8 ^{+0.4} _{-0.3}
vkdualdk	L_2 (10^3 km)	4.8 ^{+0.7} _{-0.6}	5.3 ^{+0.7} _{-0.6}	4.1 ^{+0.4} _{-0.3}	4.5 ^{+1.1} _{-0.8}	3.7 ± 0.4	3.9 ^{+0.3} _{-0.4}	4.5 ^{+0.5} _{-0.6}	4.0 ^{+0.8} _{-0.7}	2.8 ^{+1.1} _{-0.8}	3.4 ^{+0.5} _{-0.7}	3.7 ^{+0.5} _{-0.2}
	η_1	0.26 ^{+0.02} _{-0.01}	0.27 ^{+0.01} _{-0.02}	0.25 ^{+0.02} _{-0.01}	0.25 ^{+0.02} _{-0.04}	0.28 ^{+0.01} _{-0.01}	0.28 ^{+0.01} _{-0.02}	0.28 ^{+0.01} _{-0.02}	0.28 ± 0.02	0.22 ^{+0.03} _{-0.05}	0.25 ^{+0.03} _{-0.04}	0.26 ± 0.02
vkdualdk	η_2	0.35 ^{+0.02} _{-0.01}	0.34 ± 0.01	0.35 ± 0.01	0.32 ± 0.01	0.36 ± 0.01	0.36 ± 0.01	0.36 ^{+0.02} _{-0.01}	0.33 ± 0.02	0.33 ^{+0.06} _{-0.03}	0.36 ± 0.02	0.34 ± 0.01
	$\delta H_{\text{ext},1}$	7.40 ^{+0.82} _{-0.85}	6.80 ^{+0.54} _{-0.73}	10.60 ^{+1.15} _{-0.96}	9.30 ^{+1.35} _{-1.60}	6.80 ^{+0.87} _{-0.88}	7.00 ^{+0.50} _{-0.73}	6.70 ^{+0.64} _{-0.78}	5.40 ^{+0.72} _{-0.90}	7.10 ^{+1.47} _{-2.03}	8.10 ^{+1.28} _{-1.48}	9.00 ^{+0.80} _{-1.48}
vkdualdk	$\delta H_{\text{ext},2}$	1.4 ^{+0.3} _{-0.5}	1.7 ^{+0.7} _{-1.0}	1.6 ^{+0.2} _{-0.7}	1.8 ± 0.8	1.0 ± 0.1	1.5 ^{+0.5} _{-0.4}	1.4 ^{+0.5} _{-0.8}	1.7 ^{+0.8} _{-1.6}	1.1 ^{+0.6} _{-0.9}	1.1 ^{+0.3} _{-0.8}	1.6 ^{+0.3} _{-0.5}
	ϕ (rad)	-3.10 ^{+0.01} _{-0.03}	-3.13 ^{+0.05} _{-0.01}	-3.10 ± 0.02	3.13 ± 0.01	[-3] ^a	-3.09 ^{+0.05} _{-0.02}	-3.09 ^{+0.05} _{-0.02}	-3.12 ^{+0.04} _{-0.01}	-3.04 ^{+0.20} _{-0.05}	-3.07 ^{+0.08} _{-0.02}	-3.12 ^{+0.05} _{-0.02}
vkdualdk	reflag (10^{-2})	-0.8 ± 0.4	1.4 ± 0.4	4.2 ± 0.4	5.7 ± 0.7	-2.9 ± 0.5	-2.0 ± 0.4	-0.5 ± 0.5	-0.5 ± 0.9	-4.1 ± 1.5	-1.7 ± 0.8	-0.9 ± 0.6
	$\eta_{\text{ml},1}$	0.019 ^{+0.003} _{-0.002}	0.019 ^{+0.003} _{-0.002}	0.015 ± 0.001	0.014 ^{+0.003} _{-0.002}	0.017 ± 0.001	0.021 ± 0.001	0.020 ^{+0.003} _{-0.002}	0.021 ^{+0.004} _{-0.003}	0.020 ^{+0.006} _{-0.003}	0.019 ^{+0.005} _{-0.002}	0.018 ± 0.002
vkdualdk	$\eta_{\text{ml},2}$	0.027 ± 0.001	0.025 ^{+0.001} _{-0.002}	0.023 ± 0.001	0.020 ± 0.001	0.028 ^{+0.001} _{-0.000}	0.029 ± 0.001	0.028 ^{+0.001} _{-0.003}	0.026 ^{+0.002} _{-0.005}	0.030 ^{+0.002} _{-0.003}	0.030 ^{+0.001} _{-0.002}	0.026 ± 0.001
	χ^2 (dof)	264.2 (251)	250.0 (250)	266.5 (251)	221.6 (243)	208.2 (252)	235.2 (249)	216.4 (248)	214.9 (251)	197.2 (225)	215.3 (239)	214.9 (245)

Notes. Rows are defined as in Table A.2.

Table A.4. Same as Table A.2 for observation numbers 26 to 36.

Component	Parameter	Observation number										
		26	27	28	29	30	31	32	33	34	35	36
TBfeo	QPO frequency (Hz)	1.352 ± 0.005	1.397 ± 0.01	2.267 ± 0.01	2.76 ± 0.008	2.455 ± 0.008	3.154 ± 0.007	3.378 ± 0.008	2.827 ± 0.008	2.704 ± 0.005	2.606 ± 0.004	2.056 ± 0.004
	time lag (10^{-2} sec)	-0.06 ± 0.14	-0.85 ± 0.24	-1.1 ± 0.45	-1.51 ± 0.32	-0.79 ± 0.14	-1.18 ± 0.09	-1.05 ± 0.16	-0.97 ± 0.14	-0.77 ± 0.06	-0.81 ± 0.06	-0.6 ± 0.08
diskbb	N_{H} (10^{22} cm $^{-2}$)	[0.28] ^a	[0.28] ^a	[0.28] ^a	[0.28] ^a	[0.28] ^a	[0.28] ^a	[0.28] ^a	[0.28] ^a	[0.28] ^a	[0.28] ^a	
nthComp	kT_{in} (keV)	0.403 ± 0.004	0.414 ± 0.004	0.490 ± 0.006	0.512 ± 0.006	0.480 ± 0.005	0.530 ± 0.006	0.548 ± 0.008	0.518 ± 0.006	0.502 ± 0.006	0.500 ± 0.006	0.453 ± 0.005
	N_{disk}^b (10^4)	8.2 ± 0.2	7.7 ± 0.2	3.8 ± 0.1	2.5 ± 0.1	3.5 ± 0.1	1.9 ± 0.1	1.6 ± 0.2	2.8 ± 0.1	2.7 ± 0.1	2.7 ± 0.1	4.2 ± 0.1
gaussian	F_{disk}^* (10^{-8} ergs cm $^{-2}$ s $^{-1}$)	4.4 ± 0.1	4.7 ± 0.1	4.6 ± 0.3	3.6 ± 0.3	3.9 ± 0.2	3.1 ± 0.3	3.0 ± 0.5	4.2 ± 0.3	3.6 ± 0.2	3.5 ± 0.2	3.7 ± 0.2
	Γ	1.870 ± 0.005	1.845 ± 0.009	2.020 ± 0.014	2.148 ± 0.012	2.075 ± 0.010	2.223 ± 0.010	2.256 ± 0.011	2.122 ± 0.013	2.149 ± 0.011	2.172 ± 0.009	2.054 ± 0.007
vkdualdk	kT_e (keV)	[40] ^a	[40] ^a	[40] ^a	[40] ^a	[40] ^a	[40] ^a	[40] ^a	[40] ^a	[40] ^a	[40] ^a	
	N_{nthComp}	29.6 ± 0.4	28.5 ± 0.4	30.2 ± 0.8	35.2 ± 0.8	33.1 ± 0.7	38.8 ± 0.9	40.0 ± 1.4	33.8 ± 0.8	34.8 ± 0.7	33.9 ± 0.7	29.8 ± 0.5
gaussian	F_{nthComp}^* (10^{-8} ergs cm $^{-2}$ s $^{-1}$)	40.3 ± 0.2	41.6 ± 0.4	33.8 ± 0.2	33.2 ± 0.2	33.5 ± 0.1	33.9 ± 0.2	34.3 ± 0.3	33.3 ± 0.2	32.4 ± 0.2	30.6 ± 0.1	30.3 ± 0.1
	lineE (keV)	[6.4] ^a	[6.4] ^a	-	-	-	-	-	-	[6.4] ^a	-	[6.4] ^a
vkdualdk	σ (keV)	[1.0] ^a	0.7 ± 0.2	-	-	-	-	-	-	0.8 ± 0.3	-	[1.0] ^a
	Strength (10^{-1})	[2.0] ^a	1.0 ± 0.3	-	-	-	-	-	-	0.6 ± 0.3	-	[2.0] ^a
vkdualdk	kT_{S_1} (keV)	0.297 ^{+0.034} _{-0.042}	0.262 ^{+0.159} _{-0.120}	0.284 ^{+0.052} _{-0.033}	0.363 ^{+0.058} _{-0.044}	0.336 ^{+0.056} _{-0.043}	0.482 ^{+0.026} _{-0.022}	0.430 ^{+0.060} _{-0.074}	0.396 ^{+0.044} _{-0.027}	0.382 ^{+0.021} _{-0.017}	0.369 ^{+0.053} _{-0.106}	0.278 ^{+0.083} _{-0.048}
	L_1 (10^3 km)	1.8 ^{+0.3} _{-0.2}	4.1 ^{+3.9} _{-1.1}	1.1 ^{+0.9} _{-0.5}	2.4 ^{+1.2} _{-0.6}	1.9 ^{+1.4} _{-0.7}	2.1 ^{+0.5} _{-0.4}	1.9 ^{+0.3} _{-0.5}	1.1 ^{+0.5} _{-0.4}	1.7 ± 0.3	1.5 ^{+0.6} _{-0.4}	1.5 ^{+0.5} _{-0.4}
vkdualdk	L_2 (10^3 km)	2.4 ^{+0.6} _{-0.4}	4.8 ^{+4.4} _{-2.1}	[1.1] ^b	[2.4] ^b	[1.9] ^b	[2.1] ^b	[1.9] ^b	[1.7] ^b	[1.7] ^b	1.4 ^{+0.7} _{-1.0}	1.8 ± 0.5
	η_1	0.28 ^{+0.02} _{-0.04}	0.27 ^{+0.16} _{-0.09}	0.22 ^{+0.07} _{-0.05}	0.24 ^{+0.08} _{-0.10}	0.28 ^{+0.08} _{-0.09}	0.34 ^{+0.08} _{-0.04}	0.26 ^{+0.12} _{-0.02}	0.32 ^{+0.06} _{-0.03}	0.32 ± 0.03	0.33 ^{+0.02} _{-0.06}	0.27 ^{+0.06} _{-0.04}
vkdualdk	η_2	0.36 ± 0.01	0.38 ^{+0.20} _{-0.07}	0.35 ^{+0.05} _{-0.18}	0.30 ± 0.12	0.36 ± 0.08	0.36 ^{+0.07} _{-0.12}	0.01 ± 0.70	0.41 ± 0.04	0.41 ± 0.03	0.45 ^{+0.08} _{-0.04}	0.44 ^{+0.03} _{-0.04}
	$\delta H_{\text{ext},1}$	9.90 ^{+3.77} _{-2.74}	7.80 ^{+3.77} _{-11.44}	5.70 ^{+2.52} _{-3.77}	2.30 ^{+0.81} _{-0.93}	2.40 ^{+0.84} _{-1.04}	2.20 ^{+0.46} _{-0.57}	0.90 ^{+0.50} _{-1.96}	3.50 ^{+0.70} _{-0.94}	3.00 ^{+0.44} _{-0.46}	2.60 ^{+0.79} _{-1.08}	5.80 ^{+1.50} _{-1.71}
vkdualdk	$\delta H_{\text{ext},2}$	2.1 ^{+0.9} _{-0.6}	1.0 ^{+0.6} _{-1.3}	0.5 ^{+0.3} _{-0.2}	0.4 ^{+0.3} _{-0.2}	4 ^{+0.3} _{-0.4}	1.3 ^{+0.8} _{-0.6}	0.1 ^{+0.1} _{-0.3}	1.1 ± 0.3	0.8 ± 0.2	0.6 ^{+0.4} _{-1.4}	0.6 ^{+0.2} _{-0.6}
	ϕ (rad)	-3.14 ± 0.01	-3.11 ^{+0.20} _{-0.11}	[-3] ^a	[-3] ^a	[-3] ^a	[-3] ^a	[-3] ^a	[-3] ^a	[-3] ^a	[-3] ^a	-2.92 ^{+0.51} _{-0.16}
vkdualdk	reflag (10^{-2})	-0.8 ± 1.3	-5.6 ± 2.2	-9.6 ± 4.7	-12.6 ± 4.0	-10.1 ± 3.0	-16.1 ± 2.0	-13.3 ± 2.9	-16.9 ± 3.9	-12.6 ± 1.7	-12.4 ± 1.5	-9.1 ± 1.5
	$\eta_{\text{ml},1}$	0.021 ^{+0.005} _{-0.004}	0.018 ^{+0.006} _{-0.004}	0.023 ^{+0.005} _{-0.008}	0.036 ^{+0.010} _{-0.008}	0.035 ± 0.006	0.056 ± 0.006	0.044 ^{+0.004} _{-0.002}	0.044 ± 0.004	0.046 ± 0.003	0.050 ^{+0.011} _{-0.007}	0.030 ± 0.004
vkdualdk	$\eta_{\text{ml},2}$	0.028 ± 0.002	0.028 ± 0.005	0.042 ^{+0.006} _{-0.007}	0.048 ^{+0.019} _{-0.015}	0.048 ± 0.008	0.060 ^{+0.008} _{-0.006}	0.002 ^{+0.047} _{-0.001}	0.058 ± 0.005	0.061 ± 0.003	0.067 ^{+0.004} _{-0.007}	0.054 ^{+0.002} _{-0.003}
	χ^2 (dof)	211.1 (229)	210.3 (190)	144.1 (147)	157.9 (145)	164.7 (153)	159.9 (160)	115.7 (153)	155.7 (153)	193.5 (219)	263.4	

Table A.5. Same as Table A.2 for observation numbers 37 to 54.

Component	Parameter	Observation number											
		37	38	39	40	41	42	43	44	45	46	47	54
TBfeo	QPO frequency (Hz)	1.992 ± 0.003	2.308 ± 0.004	2.555 ± 0.004	2.74 ± 0.003	2.48 ± 0.004	2.531 ± 0.012	6.195 ± 0.022	6.856 ± 0.031	6.913 ± 0.021	6.84 ± 0.014	7.067 ± 0.032	6.697 ± 0.027
	time lag (10 ⁻² sec)	-0.38 ± 0.06	-0.94 ± 0.11	-1.01 ± 0.06	-1.08 ± 0.05	0.03 ± 0.08	-0.51 ± 0.42	-2.83 ± 0.17	-3.21 ± 0.36	-2.91 ± 0.18	-1.26 ± 0.06	-1.26 ± 0.21	-1.05 ± 0.12
diskbb	N_{H} (10 ²² cm ⁻²)	[0.28] ^a	[0.28] ^a	[0.28] ^a	[0.28] ^a	[0.28] ^a	[0.28] ^a	[0.28] ^a	[0.28] ^a	[0.28] ^a	[0.28] ^a	[0.28] ^a	[0.28] ^a
	kT_{in} (keV)	0.443 ± 0.003	0.463 ± 0.004	0.454 ± 0.004	0.468 ± 0.004	0.454 ± 0.004	0.484 ± 0.004	0.692 ± 0.005	0.751 ± 0.005	0.761 ± 0.004	0.753 ± 0.004	0.736 ± 0.005	0.725 ± 0.004
nthComp	N_{disk}^b (10 ⁴)	5.0 ± 0.1	3.8 ± 0.1	3.3 ± 0.1	2.9 ± 0.1	3.3 ± 0.1	3.5 ± 0.1	0.5 ± 0.1	0.6 ± 0.1	0.7 ± 0.1	0.7 ± 0.1	0.6 ± 0.1	0.8 ± 0.1
	F_{disk}^* (10 ⁻⁹ ergs cm ⁻² s ⁻¹)	5.4 ± 0.1	4.0 ± 0.1	3.6 ± 0.1	2.9 ± 0.1	2.9 ± 0.1	3.0 ± 0.2	2.4 ± 0.4	4.4 ± 0.5	5.1 ± 0.3	4.7 ± 0.3	3.8 ± 0.5	4.7 ± 0.3
gaussian	Γ	1.994 ± 0.006	2.083 ± 0.008	2.170 ± 0.006	2.183 ± 0.006	2.155 ± 0.007	2.129 ± 0.009	2.966 ± 0.017	3.050 ± 0.029	3.027 ± 0.020	3.056 ± 0.017	3.080 ± 0.030	3.025 ± 0.023
	kT_e (keV)	[250] ^a	[250] ^a	[250] ^a	[250] ^a	[250] ^a	[250] ^a	[250] ^a	[250] ^a	[250] ^a	[250] ^a	[250] ^a	[250] ^a
vkdualdk	N_{nthComp}	28.0 ± 0.3	30.7 ± 0.5	35.5 ± 0.4	34.8 ± 0.5	33.2 ± 0.5	32.5 ± 0.5	34.2 ± 0.9	30.7 ± 1.1	28.7 ± 0.8	28.8 ± 0.7	30.5 ± 1.2	24.1 ± 0.7
	F_{nthComp}^* (10 ⁻⁹ ergs cm ⁻² s ⁻¹)	21.7 ± 0.1	32.2 ± 0.1	31.1 ± 0.1	31.4 ± 0.1	30.7 ± 0.1	30.0 ± 0.1	21.4 ± 0.3	19.9 ± 0.4	18.9 ± 0.3	18.6 ± 0.3	19.1 ± 0.4	15.3 ± 0.3
gaussian	lineE (keV)	[6.4] ^a	[6.4] ^a	[6.4] ^a	[6.4] ^a	[6.4] ^a	–	–	–	–	–	–	–
	σ (keV)	0.6 ± 0.1	[0.7] ^a	0.7 ± 0.1	[0.7] ^a	[0.7] ^a	–	–	–	–	–	–	–
vkdualdk	Strength (10 ⁻¹)	0.6 ± 0.1	0.6 ± 0.1	0.5 ± 0.1	0.5 ± 0.1	0.6 ± 0.1	–	–	–	–	–	–	–
	$kT_{\text{e},1}$ (keV)	0.379 ^{+0.011} _{-0.045}	0.293 ^{+0.020} _{-0.018}	0.341 ^{+0.038} _{-0.016}	0.396 ^{+0.015} _{-0.012}	0.355 ^{+0.028} _{-0.030}	0.267 ^{+0.072} _{-0.049}	0.625 ^{+0.015} _{-0.013}	0.716 ^{+0.038} _{-0.028}	0.713 ^{+0.017} _{-0.015}	0.714 ^{+0.028} _{-0.024}	0.704 ^{+0.013} _{-0.026}	0.691 ^{+0.037} _{-0.030}
vkdualdk	L_1 (10 ³ km)	2.4 ± 0.4	0.8 ± 0.2	1.8 ^{+0.5} _{-0.3}	2.0 ^{+0.2} _{-0.3}	2.4 ^{+0.6} _{-0.5}	2.7 ^{+0.9} _{-0.8}	10.4 ^{+2.1} _{-1.5}	9.7 ^{+6.2} _{-3.5}	9.2 ^{+2.8} _{-2.0}	14.4 ^{+0.8} _{-4.9}	14.3 ^{+1.3} _{-1.9}	10.8 ^{+5.1} _{-2.1}
	L_2 (10 ³ km)	2.6 ^{+0.5} _{-0.4}	[0.8] ^b	1.9 ^{+0.7} _{-0.5}	[2.0] ^b	[2.4] ^b	[2.7] ^b	[1.9] ^a	[1.9] ^a	[1.9] ^a	[1.9] ^a	[1.9] ^a	[1.9] ^a
vkdualdk	η_1	0.25 ± 0.01	0.22 ± 0.02	0.23 ± 0.02	0.31 ± 0.02	0.28 ± 0.04	0.18 ^{+0.07} _{-0.04}	0.52 ^{+0.15} _{-0.10}	[0.59] ^c	0.57 ^{+0.23} _{-0.14}	[0.97] ^c	[0.93] ^c	[0.57] ^c
	η_2	0.28 ± 0.01	0.35 ± 0.01	0.30 ± 0.01	0.37 ^{+0.02} _{-0.01}	0.36 ^{+0.03} _{-0.04}	[0.3] ^a	[0.3] ^a	[0.3] ^a	[0.3] ^a	[0.3] ^a	[0.3] ^a	[0.3] ^a
vkdualdk	$\delta\dot{H}_{\text{ext},1}$	7.60 ^{+1.59} _{-1.79}	6.50 ^{+1.20} _{-1.60}	3.60 ^{+0.34} _{-0.85}	2.70 ^{+0.23} _{-0.29}	2.90 ^{+0.54} _{-0.48}	2.80 ^{+1.18} _{-2.06}	0.30 ± 0.03	0.20 ^{+0.05} _{-0.06}	0.30 ^{+0.03} _{-0.05}	0.30 ^{+0.05} _{-0.04}	0.30 ± 0.04	0.20 ± 0.04
	$\delta\dot{H}_{\text{ext},2}$	3.4 ^{+2.0} _{-1.9}	0.9 ± 0.1	0.9 ^{+0.3} _{-0.5}	1.2 ± 0.2	0.9 ^{+0.4} _{-0.3}	0.1 ^{+0.1} _{-0.3}	[0.9] ^a	[0.9] ^a	[0.9] ^a	[0.9] ^a	[0.9] ^a	[0.9] ^a
vkdualdk	ϕ (rad)	3.14 ± 0.01	[-3] ^a	-3.00 ^{+0.03} _{-0.11}	[-3] ^a	[-3] ^a	[-3] ^a	-3.06 ± 0.06	-3.09 ^{+0.14} _{-0.17}	-2.99 ^{+0.08} _{-0.09}	-2.78 ^{+0.15} _{-0.08}	-2.78 ^{+0.14} _{-0.05}	-2.85 ^{+0.10} _{-0.17}
	reflag (10 ⁻²)	-5.1 ± 1.1	-10.4 ± 2.0	-11.5 ± 0.4	-12.0 ± 0.9	-11.7 ± 1.4	-9.2 ± 3.9	-37.8 ± 2.2	-38.2 ± 3.1	-39.6 ± 1.1	-45.3 ± 5.5	-45.6 ± 5.5	-41.9 ± 4.9
vkdualdk	$\eta_{\text{int},1}$	0.020 ± 0.002	0.022 ± 0.001	0.030 ^{+0.003} _{-0.002}	0.040 ± 0.002	0.021 ^{+0.007} _{-0.003}	0.050 ^{+0.021} _{-0.017}	0.157 ^{+0.032} _{-0.027}	0.180 ^{+0.055} _{-0.075}	0.178 ^{+0.038} _{-0.048}	0.192 ± 0.082	0.200 ^{+0.068} _{-0.056}	0.180 ^{+0.054} _{-0.056}
	$\eta_{\text{int},2}$	0.023 ± 0.001	0.037 ± 0.001	0.038 ± 0.002	0.049 ± 0.002	0.044 ^{+0.003} _{-0.002}	[0.096] ^a	[0.089] ^a	[0.092] ^a	[0.091] ^a	[0.092] ^a	[0.093] ^a	[0.091] ^a
vkdualdk	χ^2 (dof)	267.5 (226)	171.9 (166)	239.2 (244)	210.4 (234)	172.1 (222)	148.6 (172)	140.6 (183)	137.0 (174)	149.5 (192)	119.7 (194)	128.5 (173)	176.4 (183)

Notes. Rows are defined as in Table A.2.

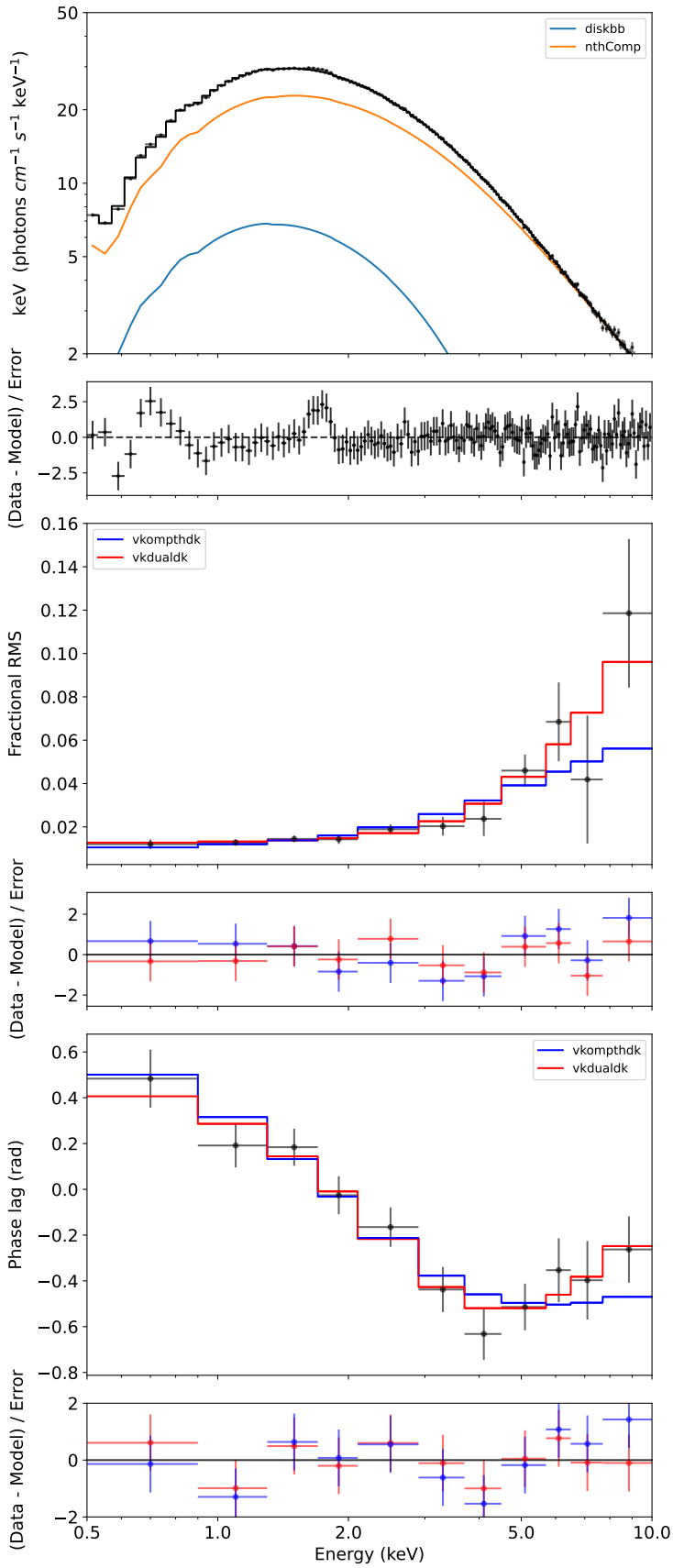


Fig. A.2. Same as Figure 6 but for observation ID 6557020402 with the type-C QPO at a centroid frequency 7.0 Hz.

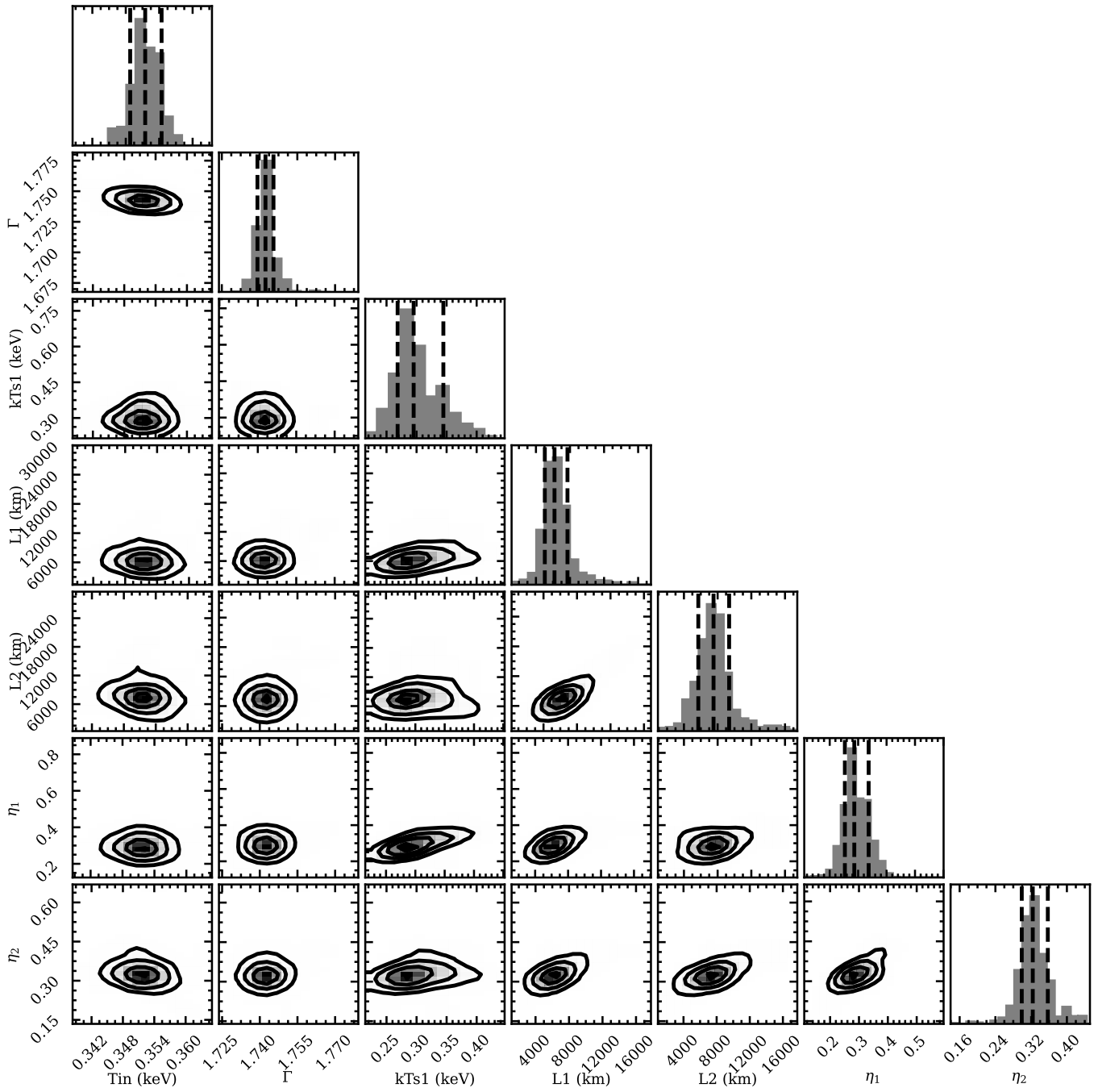


Fig. A.3. Corner plot for the parameters of Swift J1727.8-1613 for ObsID 6203980105 fitted using vkdua1dk.